Single-cell analysis of innate spinal cord regeneration identifies intersecting modes of neuronal repair.

Vishnu Muraleedharan Saraswathy[1,2], Lili Zhou[1,2] and Mayssa H. Mokalled[1,2,3]

[1] Department of Developmental Biology
Washington University School of Medicine, St. Louis, MO, USA 63110.

[2] Center of Regenerative Medicine
Washington University School of Medicine, St. Louis, MO, USA 63110.

[3] Author for correspondence: mmokalled@wustl.edu

ABSTRACT

Adult zebrafish have an innate ability to recover from severe spinal cord injury. Here, we report a comprehensive single nuclear RNA sequencing atlas that spans 6 weeks of regeneration. We identify cooperative roles for adult neurogenesis and neuronal plasticity during spinal cord repair. Neurogenesis of glutamatergic and GABAergic neurons restores the excitatory/inhibitory balance after injury. In addition, a transient population of injury-responsive neurons (iNeurons) show elevated plasticity between 1 and 3 weeks post-injury. We found iNeurons are injury-surviving neurons that acquire a neuroblast-like gene expression signature after injury. CRISPR/Cas9 mutagenesis showed iNeurons are required for functional recovery and employ vesicular trafficking as an essential mechanism that underlies neuronal plasticity. This study provides a comprehensive resource of the cells and mechanisms that direct spinal cord regeneration and establishes zebrafish as a model of plasticity-driven neural repair.

INTRODUCTION

Mammalian spinal cord injuries (SCI) elicit complex multi-cellular responses that impede regeneration and cause permanent functional deficits in mammals (Brennan and Popovich, 2018; Fouad et al., 2021; He and Jin, 2016; Milich et al., 2019; Sofroniew, 2018; Tran et al., 2022). Anti-regenerative neuron-extrinsic factors comprise chronic inflammation, fibrotic scarring, demyelination and the acquisition of a regeneration restricting extracellular milieu. These injury complications exacerbate the inherently limited ability of the mammalian spinal cord (SC) to replenish lost neurons via adult neurogenesis or to regrow lesioned axon tracts. Consequently, even the most groundbreaking regenerative therapies targeting select cell types or individual molecules have only yielded modest improvement in cellular and functional outcomes (Park et al., 2008; Sofroniew, 2018). SCI studies have since pursued combinatorial strategies as a more promising therapeutic avenue (Anderson et al., 2018; DePaul et al., 2017; Nakamura et al., 2021; Squair et al., 2023). We propose that comprehensive and simultaneous examination of neuronal and non-neuronal cells after SCI is fundamental to understanding and manipulating the multi-cellular complexities of neural injuries.

Unlike mammals, adult zebrafish have an innate ability to spontaneously recover from severe SCI. Following complete transection of SC tissues, zebrafish reverse paralysis and regain swim function within 6 to 8 weeks of injury (Burris et al., 2021; Mokalled et al., 2016). Pro-regenerative injury responses involving immune and progenitor cells, neurons and glia, cooperate to achieve spontaneous and efficient repair in zebrafish (Briona et al., 2015; Cavone et al., 2021; Klatt Shaw et al., 2021; Kuscha et al., 2012; Reimer et al., 2008; Saraswathy et al., 2022; Vandestadt et al., 2021). Early after SCI, potent populations of progenitor cells, including central canal-surrounding ependymo-radial glial cells (ERGs), are activated to replenish lost neurons and glia (Briona *et al.*, 2015; Klatt Shaw *et al.*, 2021; Reimer *et al.*, 2008; Saraswathy *et al.*, 2022). Newly differentiated motor neurons and interneurons populate the regenerate tissue, as pre-existing neurons regrow axons across lesioned tissues (Kuscha *et al.*, 2012; Reimer *et al.*, 2008; Saraswathy *et al.*, 2022). Though less studied, glial cells are thought to enact instrumental pro-regenerative responses throughout the course of regeneration (Goldshmit et al., 2012; Klatt Shaw *et al.*, 2021; Mokalled *et al.*, 2016). However, a holistic understanding of the cellular interactions that coordinate the pro-regenerative responses to direct SC regeneration in zebrafish is to be acquired.

The advent of single-cell transcriptomics provided the tools to achieve a refined understanding of molecular SCI responses across species and cell types. Multiple single-cell RNA sequencing

(scRNA-seq) atlases have been generated for mouse SCI, rat SCI or human SC tissues (Matson et al., 2022; Milich et al., 2021; Rodrigo Albors et al., 2023; Yadav et al., 2023; Yao et al., 2022). Single-cell studies from mice revealed new insights into macroglial cell-cell interactions after injury, revealed a rare population of lumbar spinocerebellar neurons that elicit a regeneration signature, or characterized the responses of astrocytes after injury (Hou et al., 2022; Matson *et al.*, 2022; Milich *et al.*, 2021; Rodrigo Albors *et al.*, 2023). However, single-cell studies from zebrafish SC tissues have been limited to isolated immune or progenitor motor neuron cells and to larval stages (Cavone *et al.*, 2021; Scott et al., 2021). Thus, a complete resource of the regenerative cells and mechanisms from adult zebrafish is required to develop a molecular understanding of the cell identities that enable or limit spontaneous plasticity and regeneration.

The fundamental principles that determine or limit regenerative capacity across species have eluded scientists for ages. While pro-regenerative injury responses are overwhelmed by anti-regenerative complications in mammals, zebrafish cells exhibit increased potency and exclusively pro-regenerative signatures after SCI. Molecular and cellular studies of select cell types or regenerative pathways revealed key insights into the cellular contributions and molecular signatures associated with elevated regenerative capacity. Specifically, while ependymal cells elicit limited stem cell potential in adult mice (Ren et al., 2017; Shah et al., 2018), zebrafish ERGs retain radial glial features and contribute to neurogenesis and gliogenesis after SCI (Briona *et al.*, 2015; Klatt Shaw *et al.*, 2021; Reimer *et al.*, 2008; Saraswathy *et al.*, 2022). The disparities in neuron progenitor capacities between zebrafish and mammals yielded an assumption that neurogenesis-based neural repair is unachievable in mammals and directed the community's efforts toward plasticity-based neural repair strategies. However, while zebrafish has been an established model of neuron regeneration, it remains unclear whether zebrafish could contribute insights and applications into plasticity-driven repair mechanisms. Thus, how and why neuronal injury responses differ between zebrafish and mammals require comprehensive molecular investigation and cross-species comparisons.

This study presents an atlas of the dynamic responses across major spinal cell types during early, intermediate and late stages of regeneration in adult zebrafish. Single nuclear RNA sequencing (snRNA-seq) was performed at 0, 1, 3 and 6 weeks post-injury. Neurons elicit elevated signaling activity relative to the dozens of cell types that respond to injury. While SCI disrupts the excitatory/inhibitory neuron balance, sequential neurogenesis of excitatory and inhibitory neurons restores the homeostatic neuronal landscape at late stages of regeneration. In

64 addition to regenerating new neurons, a transient regenerative signature emerges in a population
65 of injury-responsive neurons (iNeurons) between 1 and 3 weeks post-injury. EdU labeling showed
66 iNeurons are injury surviving neurons that acquire a neuroblast-like transcriptional signature after
67 injury. iNeuron markers genes are required for functional SC repair, and dynamic vesicular
68 trafficking is a central mechanism that promotes spontaneous neuronal plasticity. This study
69 identifies multi-layered modes of regenerative neurogenesis and neuronal plasticity during innate
70 SC regeneration, and establishes zebrafish as a platform to identify and manipulate regeneration-
71 and plasticity-based modes of neural repair.

RESULTS

72 **Molecular identification and temporal dynamics of spinal cell types after injury.**
73 To determine the transcriptional identities of the cells that directs successful SC regeneration, we
74 performed complete SC transections on adult zebrafish and dissected 3 mm sections of SC
75 tissues surrounding the lesion site at 1, 3, and 6 weeks post-injury (wpi) for nuclear isolation.
76 Corresponding tissue sections were collected from uninjured controls. SC tissues were pooled
77 from 50 animals per time point, and 2 pools of independent biological replicates were analyzed
78 for each time point. Our dataset spans key regenerative windows including early injury-induced
79 signals at 1 wpi, neuronal and glial regeneration at 3 wpi, and cellular remodeling at late stages
80 of regeneration at 6 wpi (Mokalled *et al.*, 2016). Isolated nuclei were sequenced using 10x
81 genomics platform (3' v3.1 chemistry) and aligned to zebrafish genome GRCz11 with improved
82 zebrafish transcriptome annotation (Lawson et al., 2020; Matson et al., 2018). Nuclei were
83 subsequently filtered using the Decontx and DoubletFinder packages to exclude droplets that
84 include doublet nuclei or a high proportion of ambient mRNA, respectively (McGinnis et al., 2019;
85 Yang et al., 2020). A second round of filtering is performed by thresholding the covariates such
86 as number of counts, genes and fraction of counts from mitochondrial genes per barcode. A total
87 of 58,973 nuclei was obtained for downstream analysis using the Seurat package (Fig. 1A and
88 S1A-C).

89 Clustering of SC nuclei revealed 24 cell clusters with distinct molecular identities and temporal
90 dynamics (Fig. S1D and Table S3). Postulating that previously established cell type classifiers
91 are likely biased toward cell identities present in the mammalian nervous system or in developing
92 zebrafish, we optimized cell type identification by generating a custom-assembled Vertebrate
93 CNS Marker (VNM) database. VNM compiled cell type markers commonly present in the central

nervous system from over 12 datasets and from vertebrate species including zebrafish, mice and humans (Table S1) (Baek et al., 2019; Cavone *et al.*, 2021; Guillemot, 2007; Haring et al., 2018; Hayashi et al., 2018; Hernandez-Miranda et al., 2017; Lu et al., 2015; Milich *et al.*, 2021; Rosenberg et al., 2018; Rougeot et al., 2019; Sathyamurthy et al., 2018; Tambalo et al., 2020; Tang et al., 2017; Zeisel et al., 2018; Zhang et al., 2014). We then cross-referenced differentially expressed (DE) markers for each cluster with our VNM database (Table S2 and Fig. S1E). Scoring matrix heatmap representation of this analysis identified 6 major cell types comprising neurons, glia/ERGs, oligodendrocyte precursor cells (OPCs), oligodendrocytes, leukocytes and erythrocytes. Two distinct cell populations were identified for neurons (Neurons A and B), oligodendrocytes (Oligos A and B) and Leukocytes (Leukocytes A and B). Additional subclusters within each major cell population were further identified using the prediction from scoring matrix heatmap (Fig. 1B and S1E). VNM-based cell type classification was further confirmed by evaluating the expression of canonical marker genes for each cluster (Fig. 1C). *elavl3* and *snap25a* were enriched in Neurons A and B, *gfap* and *slc4a10a* in glia/ERGs, *cspg4* and *sema5a* in OPCs, *mpz* and *mbpa* in oligodendrocytes A, *csfr1a* and *ptprc* in leukocytes A, *hbba1* in erythrocytes (Fig. 1C and S1G). Although canonical cell markers were enriched in their respective clusters, the proportions of cells expressing these markers in leukocytes A, glia/ERGs and erythrocytes were relatively small. On the other hand, gene expression analysis of Neurons B, Oligodendrocytes B and Leukocytes B did not show enrichment for classical markers. We conclude that our VNM database is likely still biased toward commonly used mammalian cell markers that are not necessarily the best markers for adult zebrafish, and that our single-cell atlas provides a platform to identify improved CNS markers for adult zebrafish cells. To test this hypothesis, we examined whether our snRNA-seq dataset identified improved cell-specific DE markers in adult zebrafish SCs (Fig. 1E). We found that Glia/ERG cells expressed the cilia-associated *cfap57* gene, indicative of the ciliated nature of the SC central canal-lining ERGs. Neurons B expressed *pkd2l1* and *pkd1l2a*, which are known markers of cerebrospinal fluid-contacting neurons (Sternberg et al., 2018). Oligodendrocytes B expressed *scn4ab* and *gfra1a*. Leukocytes A were enriched for *mrc1b* and *slco2b1* along with the cell adhesion molecule coding *mcamb* gene, whereas Leukocytes B expressed unknown genes such as *si:dkey-241l7.2* and *si:dkey-241l7.4*. These studies indicated that extrapolating mammalian CNS or developmental zebrafish markers in adult zebrafish requires validation, and provided a platform to identify new and improved CNS cell markers in adult zebrafish.

126 To examine the temporal dynamics of SC cells during regeneration, we determined the
127 numbers and relative proportions of nuclei within each coarse cluster in the integrated dataset
128 (Fig. 1D and S1F). Neurons A, which comprised 32% of the nuclei harvested from uninjured SCs,
129 comprised 18% of total nuclei at 1 wpi and recovered to 25% at 6 wpi. Neurons B represented a
130 smaller proportion of neurons and showed little variation during the course of regeneration. The
131 proportions of leukocytes A increased from 6% of control nuclei prior to injury to 20% at 1 wpi and
132 gradually decreased to 14% at 6 wpi. We observed an expansion in the relative abundance of
133 glia/ERGs between 1 and 3 wpi, whereas OPCs maintained similar proportions at all time points.
134 Oligodendrocytes A, which accounted for 18% of uninjured nuclei, gradually increased to 25% of
135 total nuclei at 6 wpi. In contrast, Oligodendrocytes B cells were transiently present at 1 wpi and
136 comprised 2% of total nuclei at that time point. These studies provided a comprehensive resource
137 of the cellular architecture that directs successful SC regeneration and revealed a gradual
138 recovery in neuronal proportions during innate SC repair.

139 **Neurons are active signaling hubs during spinal cord regeneration.**
140 To infer molecular modes of intercellular communication during SC regeneration, we surveyed
141 signaling pathways that are differentially active between 0 and 6 wpi (Fig. 2 and S2). We first
142 converted our dataset of zebrafish genes to their human orthologues using the BioMart package
143 from Ensembl. The R package "CellChat" was then used to quantitatively analyze global
144 intercellular communication networks based on the expression of ligands, receptors and cofactors
145 (Jin et al., 2021). CellChat computes the communication probabilities of ligand-receptor
146 interactions associated with each signaling pathway, and integrates the cumulative probabilities
147 of all signaling pathways that are outgoing or received (incoming) by each cell population. In
148 control SC tissues, the cumulative strengths of all signaling pathways outgoing from Neurons A
149 and B were the highest relative to other cell types, indicating active neuronal signaling under
150 homeostatic conditions (Fig. 2A-B). After SCI, outgoing signaling increased in most cell types,
151 indicating tissue-wide responses are activated after injury (Fig. 2A-B). Notably, the strengths of
152 signaling pathways outgoing from Neurons A and B continued to be elevated across all time points
153 and increased more than 2.5 fold between 0 and 6 wpi (Fig. 2A-B). On the other hand, the
154 cumulative strengths of all incoming signaling pathways received by OPCs were the highest
155 among spinal cell types after SCI (Fig. S2A and 2B). Incoming signaling received by Neurons A
156 doubled between 0 and 6 wpi (Fig. 2B). Mapping of ligand-receptor interactions predicted cell-cell
157 signaling interactions are highest between neurons and OPCs at 6 wpi (Fig. 2C). Confirming
158 CellChat analysis, trajectory inference showed OPCs and neurons have elevated transcriptional

159 activity during SC regeneration (Gulati et al., 2020) (Fig. S2B). These results indicated neurons
160 and OPCs have elevated and dynamic transcriptional and signaling activities during zebrafish SC
161 regeneration.

162 **Global and neuron-specific analyses of injury-induced signaling pathways.**
163 Global CellChat analysis revealed active signaling pathways in control, 1, 3 and 6 wpi SC tissues.
164 Tracking the strengths of individual signaling pathways across time points indicated dynamic
165 intercellular communication during SC regeneration (Fig. 2A and S2A). In addition to dynamic
166 regulation of signaling pathways present in control SC tissues, 7 pathways were specifically
167 activated at 1, 3 or 6 wpi relative to uninjured controls. Globally-induced signaling pathways
168 included chemokine signaling (CXCL), cell adhesion signaling networks (FN1 and ESAM),
169 extracellular matrix (ECM) and growth factor mediated signaling networks (SEMA6 and PDGF)
170 and developmental signaling pathways (FGF) (Fig. 2A and S2A).

171 To identify molecular pathways that account for elevated neuron signaling, we analyzed
172 signaling pathways predicted to be outgoing from or received by Neurons A and B (Fig. 2D and
173 S2C). Including both incoming and outgoing signaling, 32 to 35 pathways were predicted to be
174 activated by neurons between 0 and 6 wpi (Fig. S2C). In addition to homeostatic signaling
175 pathways increasing in strengths after injury, 5 injury-induced pathways were either activated or
176 received by neurons after injury (FGF, WNT, PDGF, FN1 and SEMA6) (Fig. 2D). SCI triggered
177 reactivation of growth factor and developmental signaling, substantiating FGF, WNT and PDGF
178 as regulators of neuron survival, axon regrowth and synapse formation (Cardozo et al., 2017;
179 Diez Del Corral and Morales, 2017; Garcia et al., 2018; Goldshmit *et al.*, 2012; Guo et al., 2019;
180 He et al., 2018; Shimada et al., 2016; Tome et al., 2023; Tsata et al., 2021; Ye et al., 2021).
181 Specifically, Neurons B are a major source of FGF18, which is predicted to interact with multiple
182 FGFR1/2/3-expressing spinal cells populations. On the other hand, Neurons A are predicted
183 recipients of WNT signaling, whereas both Neurons A and B are at the receiving end of PDGF
184 signaling. Ligand-receptor interactions involve WNT7A-FZD2/6/LRP5 and PDGFA-PDGFRB,
185 whereby Glia/ERG- and OPC-derived WNT7A and PDGFA are received by FZD2/6/LRP5- and
186 PDGFRB-expressing neurons. Highlighting the requirement for extracellular matrix (ECM)
187 remodeling and signaling to enact a pro-regenerative response (Bradbury et al., 2002; Monaghan
188 et al., 2007; Zavvarian et al., 2021), multiple cell types including Neurons A express Fibronectin
189 1 (FN1), which is predicted to direct strong interactions with SDC4-, ITGAV-, ITGA5- and ITGB1-
190 expressing cells. Conversely, Glia/ERGs are a major source of outgoing SEMA6A signaling,

191 received by PLXNA4-expressing neurons to regulate axon guidance (Carulli et al., 2021; Runker
192 et al., 2008; Squair *et al.*, 2023; Syed et al., 2016; Yoshida, 2012). These studies revealed
193 complex multicellular communication networks that coordinate signaling between neurons, glia,
194 and non-neural injury-responding cells during SC repair. Further validation and mechanistic
195 insights into these signaling pathways are required to understand their exact function during
196 zebrafish SC regeneration.

197 **Neuronal E/I balance is restored during successful spinal cord repair.**
198 To explore the cellular dynamics that support neuronal repair and functional recovery after SCI,
199 we examined neuronal cell types and states prior to and after injury. Subcluster analysis identified
200 30 distinct neuron clusters between 0 and 6 wpi (Fig. 3A, S3A-B and Table S4). Balanced synaptic
201 excitatory and inhibitory (E/I) transmission is a central feature of CNS function as altered E/I
202 balance results in severe behavioral defects in humans (Isaacson and Scanziani, 2011). Despite
203 eliciting features of cellular regeneration, SCI in mouse neonates causes impaired locomotor
204 recovery due to imbalanced E/I transmission (Bertels et al., 2022; Dudek and Sutula, 2007; Gao
205 and Penzes, 2015). With zebrafish recovering swim function after SCI, we postulated that
206 balanced E/I transmission is a hallmark of functional SC repair in zebrafish. To test this
207 hypothesis, we first performed a bioinformatic characterization of the excitatory and inhibitory
208 neurotransmitter properties of the neuron clusters identified in our dataset (Fig. 3B). Gene
209 expression for classical markers of glutamatergic (slc*17a6a, slc17a6b*), GABA/glycinergic
210 (*slc6a5, gad1a, gad1b, gad2*), cholinergic (*chata, slc5a7a*), serotonergic (*slc6a4a, tph2*) and
211 catecholaminergic (*slc6a2*) neurons were analyzed (Horzmann and Freeman, 2016) (Fig. S3C).
212 Neuron subclusters were then grouped as excitatory, inhibitory or 'Other' based on their
213 neurotransmitter gene expression profiles (Fig. 3B and S3C-E). The proportions of excitatory
214 (30%) was lower than inhibitory (56%) neurons in uninjured SC tissues (Fig. 3C), resulting in a
215 baseline E/I ratio of 0.5 (Fig. 3D). The profile of excitatory neurons increased to 34% of total
216 neurons at 1 wpi and returned to baseline levels at 6 wpi. Inhibitory neurons did not change in
217 proportions at 1 wpi but gradually increased to 60% at 6 wpi, suggesting a compensatory
218 mechanism for early surge in excitatory neurons in the injured spinal cord (Fig. 3C). *in silico*
219 calculation of the E/I ratio confirmed an imbalance toward an excitatory phenotype at 1 wpi and
220 recovery to baseline by 6 wpi (Fig. 3D).

221 To validate our bioinformatic E/I balance calculations *in vivo*, we generated dual transgenic
222 reporter fish that simultaneously label glutamatergic excitatory neurons (*vglut2a*:RFP) and

223 GABAergic inhibitory neurons (*gad1b*:GFP) (Satou et al., 2013). Complete SC transections were
224 performed on double transgenic animals and SC tissues were collected for histological
225 examination at 0, 1, 3 and 6 wpi (Fig. 3E-F). Absolute numbers and relative proportions of RFP-,
226 GFP- and HuC/D-expressing neurons were quantified in SC cross sections at 450 μm rostral to
227 the lesion to evaluate the E/I landscape during regeneration. Compared to control SC tissues, the
228 profiles of *vglut2a*$^+$ excitatory neurons (*vglut2a*$^+$ HuC/D$^+$) doubled in proportion at 1 wpi and were
229 maintained near 1 wpi levels until 6 wpi (Fig. 3G and S3F). On the other hand, the profiles of
230 *gad1b*$^+$ inhibitory neurons (*gad1b*$^+$ HuC/D$^+$) increased by 50% at 6 wpi relative to controls (Fig.
231 3H and S3G). Notably, the absolute numbers of HuC/D$^+$ neurons drastically increased at 1 and 3
232 wpi, indicating extensive neuronal remodeling during SC regeneration (Fig. S3H). Thus,
233 consistent with our snRNA-seq findings, *in vivo* studies confirmed an early surge in excitatory
234 neurons at 1 wpi and a recovery of the E/I balance toward baseline levels by 6 wpi (Fig. 3I).

235 **Neurogenesis of excitatory and inhibitory neurons after spinal cord injury.**
236 We explored the cellular bases behind the recovery of E/I balance during zebrafish SC repair.
237 The observed E/I ratio changes could be due to sequential neurogenesis of excitatory then
238 inhibitory neurons after SCI. Alternatively, E/I ratios could reflect plasticity and changes in the
239 neurotransmitter properties of pre-existing neurons. To distinguish between these possibilities,
240 we first performed a cell proliferation assay. Dual transgenic fish for *vglut2a*:RFP and *gad1b*:GFP
241 were subjected to SCI and a single EdU pulse for 24 hrs prior to SC tissue collection. SC tissues
242 were harvested at 1, 3 and 6 wpi for co-labelling with the proliferation marker EdU (Fig. 4A-B and
243 S4A). SC tissues from uninjured animals that received a single EdU injection for 24 hrs were
244 harvested as controls. In striking manifestation of the regenerative capacity of zebrafish SC
245 tissues after SCI, EdU incorporation was markedly elevated at 1 wpi relative to 0, 3 and 6 wpi
246 (Fig. 4C and S4B). The profiles and absolute numbers of newly generated glutamatergic neurons
247 (*vglut2a*$^+$ EdU$^+$) peaked at 1 wpi relative to control, 3 or 6 wpi SC sections (Fig. 4D and S4C),
248 supporting a surge of regenerating excitatory neurons at 1 wpi. As the profiles of GABAergic
249 neurons showed a gradual increase up to 6 wpi (Fig. 3H) and due to low numbers of EdU$^+$ cells
250 at 3 and 6 wpi, we were unable to evaluate the profiles of newly generated GABAergic neurons
251 with a single EdU pulse (Fig. 4E and S4D).

252 To overcome this limitation and evaluate the numbers of regenerating glutamatergic and
253 GABAergic neurons after SCI, we performed SC transections on *vglut2a*:RFP and *gad1b*:GFP
254 dual transgenic fish followed by daily EdU injections for 1 or 3 wpi (Fig. 4F-G and S4E). Uninjured

255 control animals received daily EdU injections for 1 week prior to SC tissue collection. Compared
256 to single EdU pulses, daily EdU labeling allowed us to estimate the total and cumulative profiles
257 of regenerating neurons. To account for anatomical differences along the proximo-distal axis of
258 lesioned SC tissues, RFP-, GFP- and EdU-expressing cells were quantified from SC sections
259 150, 450 and 750 μm rostral to the lesion. The numbers and proportions of EdU^+ cells sharply
260 increased at 1 wpi and showed less pronounced additive EdU incorporation at 3 wpi (Fig. S4F-
261 G). The profiles of newly formed glutamatergic (EdU^+ *vglut2a*$^+$) neurons markedly increased at 1
262 and 3 wpi relative to controls (Fig. 4H and S4H). The profiles of regenerating GABAergic (EdU^+
263 *gad1b*$^+$) neurons were significantly elevated at 1 wpi compared to controls, and continued to
264 increase at 3 wpi compared to 1 wpi (Fig. 4I and S4I). As proximal tissue sections (150 μm from
265 lesion) showed elevated neurogenesis across time points, differential dynamics of glutamatergic
266 and GABergic neuron regeneration were most prominent in more distal SC sections (750 μm from
267 lesion) (Fig. 4H and 4I). At these levels, the profiles of newly formed glutamatergic (EdU^+ *vglut2a*$^+$)
268 neurons sharply increased at 1 wpi and stabilized between 1 and 3 wpi (Fig. 4H), whereas
269 GABAergic (EdU^+ *gad1b*$^+$) continuously increased from 1 to 3 wpi (Fig. 4I). These *in vivo* studies
270 showed glutamatergic neurogenesis precedes a continuous and slower regeneration timeline for
271 GABAergic neurons, suggesting that sequential neurogenesis of different neuron subtypes
272 around the lesion accounts for the dynamic changes in E/I properties during zebrafish SC
273 regeneration.

274 **Identification of injury-responsive iNeurons during early stages of spinal cord repair.**
275 To delve into the distribution of specific neuronal populations prior to and after SCI, we calculated
276 the numbers and relative proportions of each neuron subcluster between 0 and 6 wpi (Fig. 5A,
277 3A and S3A-B). We also applied established marker genes for zebrafish larval neurons (Cavone
278 *et al.*, 2021) onto our marker scoring algorithm, identifying 7 major neuron subpopulations with
279 varying cellular dynamics during regeneration (Fig. 5B, S5A-C and Table S8). Out of 30 neuronal
280 clusters identified in our integrated dataset, cell proportions decreased >2-fold in 9 clusters (N0,
281 5, 10, 14, 15, 24, 25, 28 and 29), representing interneurons, V0, V2a interneurons, and motor
282 neurons. On the other hand, 4 neuronal clusters expanded >2-fold after SCI (N18, 20, 23 and 27)
283 (Fig. 5A). The numbers and proportions of N18 neurons increased 2.5-fold at 3 wpi and returned
284 to control levels at 6 wpi (Fig. 5A). Consistent with delayed GABAergic neurogenesis (Fig. 3 and
285 4), Cluster N18 cells were identified as GABAergic V2b interneurons (Fig. 3B and 5B). The profiles
286 of N20 neurons sharply increased 6.7-fold at 1 wpi compared to all other time points. Intriguingly,
287 N20 was the only neuron cluster corresponding to neuroblast-like neurons, suggesting a pro-

288 regenerative role for N20 neurons after SCI (Fig. 5A-B and S5A). Yet, the exact identities and role
289 of N20 during SC repair are unknown. N23 neurons were injury-induced, accounting for 2% of
290 total neurons at 1 wpi and decreasing to 0.6% of neurons at 6 wpi (Fig. 5A). N23 neurons were
291 identified as motor neurons, which are known to regenerate via neurogenesis in adult zebrafish
292 (Reimer *et al.*, 2008). N27 neurons increased 2.9-fold at 1 wpi compared to other time points and
293 were identified as serotonergic interneurons (Fig. 3B and 5B). We conclude that cluster N27
294 corresponds to intraspinal serotonergic neurons, which promote excitatory axon regrowth and
295 coordinated locomotor recovery in zebrafish (Huang et al., 2021). This analysis revealed known
296 and unanticipated neuronal dynamics during innate SC repair.

297 To estimate the regenerative potential of spinal neurons after SCI, we assigned a
298 "regeneration score" to individual neuron clusters by cross referencing the DE markers for each
299 cluster with a compiled list of regeneration associated genes. RAGs were defined based on their
300 association with the GO term "regeneration" in the Amigo database
301 (http://amigo.geneontology.org/amigo/landing) (Tables S4 and S5). Strikingly, compared to all
302 other neuron subtypes, cluster N20 showed the highest regeneration score (Fig. 5C and S5D)
303 and expressed known RAG genes including *gap43* and *atf3* (Fig. 5D) (Curtis et al., 1993; Doster
304 et al., 1991; Gey et al., 2016; Jankowski et al., 2009; Jing et al., 2012; Kole et al., 2020; Wang et
305 al., 2017; Wang et al., 2015; Williams et al., 2015; Zhang et al., 2005). Gene ontology
306 comparisons showed that terms associated with neuron development, synaptic organization and
307 axon extension were enriched in N18, 20, 23 and 27 (Fig. S5E). However, regeneration
308 associated gene enrichment was most pronounced and most significant for cluster N20 (Fig.
309 S5E). We propose that cluster N20 represents a new, transient and unique population of injury-
310 responsive neurons (iNeurons) that are likely to contribute to functional SC repair.

311 **iNeurons are signaling hubs during spinal cord regeneration.**
312 To evaluate the role of N20 iNeurons during SC regeneration, we determined the extent and
313 identities of the signaling pathways that are initiated and received by iNeurons using CellChat. To
314 specifically identify iNeurons (N20 cells) within the rest of the SC microenvironment, we first
315 tracked and identified iNeurons in the integrated dataset that includes all SC cells (Fig. S5D).
316 Cells from clusters 5 and 4 from the integrated dataset accounted for the majority of iNeurons and
317 were renamed iNeurons for CellChat analysis. Strikingly, compared to the global cell-interactions
318 derived from the integrated dataset, the cumulative and reciprocal signaling strengths were
319 highest between iNeurons and OPCs at 1 wpi (Fig. 5F). The cumulative strengths of outgoing and

320 incoming signaling were markedly lower in the rest of the neuronal cells compared to iNeurons
321 (Fig. 5F). These findings suggest that iNeuron signaling accounts for the majority of neuronal
322 signaling at 1 wpi.

323 To examine the molecular features of the crosstalk between iNeurons and OPCs, we identified
324 major signaling networks that are either incoming or outgoing from iNeurons (Fig. 5G and S5F-
325 G). CellChat analysis showed iNeurons have a high probability to transduce NCAM1/2, and
326 NRXN3 signaling to OPCs and other neurons. TIGIT, NRXN1/2, CDH4 and CADM1/3 were also
327 predicted as incoming and outgoing iNeuron signals. Consistent with the ontology of iNeuron
328 expressed genes, we observed an enrichment for reciprocal Neuregulin (NRG)-ERBB signaling
329 from iNeurons to OPCs. ErbB signaling was recently shown to regulate OPC transformation and
330 spontaneous remyelination after SCI in mice (Bartus et al., 2019). We found NRG1 and NRG2
331 ligands activate of the ERBB3/4 receptor mediated signaling between iNeurons and OPCs (Fig.
332 6D). These results showed iNeurons are potent centers of molecular signaling during SC
333 regeneration and suggested that reciprocal signaling between iNeurons and OPCs is a principal
334 feature of innate SC repair.

335 ***in vivo* mapping of iNeurons during SC regeneration.**
336 To validate the emergence of an iNeuron transcriptional signature in regenerating SC tissues, we
337 performed HCR *in situ* hybridization for select markers that are uniquely expressed in iNeurons
338 compared to all other spinal cell types in the integrated dataset (Fig. S6A). To enable differential
339 labeling of regenerating and pre-existing neurons, wild-type fish were subjected to SCI and daily
340 EdU injections. *syt11b* and *vamp4* HCR *in situ* hybridization and staining for HuC/D and EdU were
341 performed at 0, 1 and 3 wpi (Fig. 6A and 6D). To test whether iNeuron markers are preferentially
342 expressed in neurons, integrated densities of *in situ* hybridization signals were quantified in total
343 SC tissues and in HuC/D$^+$ neurons (Fig. 6A-F and S6B-H). At 1 wpi, *synaptotagmin XI b (syt11b)*
344 expression increased 3.6-fold in total SC tissues and 4.3-fold in HuC/D$^+$ neurons (Fig. 6B-C).
345 *syt11b* expression was reduced to wild-type levels by 3 wpi (Fig. 6B-C). *vesicle-associated*
346 *membrane protein 4 (vamp4)* transcripts were upregulated at 1 and 3 wpi, with 2.3- to 2.5-fold
347 increase in total SC tissues and HuC/D$^+$ neurons at 1 wpi (Fig. 6E-F). Since *syt11b* showed robust
348 expression and upregulation in neurons and to address putative redundancy between the *syt11b*
349 and *syt11a* paralogs, we examined *syt11a* expression after SCI (Fig. S6E-H). Like *syt11b*, *syt11a*
350 transcripts were upregulated after injury, including in neurons. However, unlike *syt11b*, *syt11a*
351 expression was not restricted to neurons including expression in ependymal cells surrounding the

352 central canal at 1 wpi (Fig. S6E). These findings validated *syt11b* and *vamp4* as markers of
353 zebrafish iNeurons during SC regeneration.

354 **iNeurons are surviving neurons that elicit spontaneous plasticity after injury.**
355 The emergence of an iNeuron transcriptional profile at 1 wpi raised a central question related to
356 their cell of origin and pro-regenerative signature. We postulated that iNeurons could either
357 represent newly formed regenerating neurons, or a population of spontaneously plastic neurons
358 that survive injury and support immediate repair. To distinguish between these possibilities, we
359 quantified the profiles of iNeurons that express *syt11b/a*, HuC/D and EdU (Fig. 6G-I and S6F-H).
360 In these experiments, HuC/D$^+$ EdU$^+$ represent regenerating neurons and HuC/D$^+$ EdU$^-$ represent
361 pre-existing neurons. Expectedly, the profiles of regenerating neurons significantly increased from
362 1 to 3 wpi, indicating potent neurogenic responses are activated during innate SC repair (Fig. 6H).
363 At 1 wpi, *syt11b* transcripts labeled 14.5% of HuC/D$^+$ neurons (Fig. 6G), and only 6.4% of
364 regenerating neurons (Fig. 6I). These results indicated that over 90% of iNeurons are pre-existing
365 neurons that survive SCI.

366 Since the majority of iNeurons are pre-existing in control SC tissues, we examined whether
367 iNeurons represent a specific population of neurons with elevated survival capacity or
368 spontaneous plasticity. To address this question, we performed *syt11b* HCR *in situ* hybridization
369 on *vglut2a*:RFP and *gad1b*:GFP dual transgenic fish, which simultaneously label glutamatergic
370 and GABAergic neurons (Fig. 6J). Neuron subtypes not labeled with *vglut2a*:RFP or *gad1b*:GFP
371 were labeled as others. The integrated density of *syt11b* transcript signals broadly increased at 1
372 wpi (Fig. S6I), including upregulated expression in *vglut2a*$^+$ and *gad1b*$^+$ neurons at 1 wpi (Fig.
373 S6J-K). Notably, only 37.5% and 20.7% of the combined *syt11b* signal co-localized to
374 glutamatergic and GABAergic neurons at 1 and 2 wpi, indicating that "other" neuron subtypes
375 express the majority of *syt11b* during regeneration (Fig. 6K). We also performed *syt11b* HCR *in*
376 *situ* hybridization along with Hb9, *isl1:GFP* or Pax2 staining (Fig. S6L), and found that 30-40% of
377 Hb9$^+$, *isl1:GFP*$^+$ and Pax2$^+$ neurons expressed *syt11b* at 1wpi (Fig. S6M). These findings
378 indicated that iNeurons do not represent a specific neuron subtype and suggested that multiple
379 zebrafish neurons survive SCI and elicit an iNeuron transcriptional and regenerative signature
380 during early stages of SC repair.

381 **iNeurons are integrated in the spinal circuitry after spinal cord injury.**

382 We performed two sets of tracing experiments to trace axons projecting across the lesion using
383 either rostral (Fig. 7A-C) or caudal labeling (Fig. S7A-C) with Biocytin at 1 wpi. For rostral labeling,
384 a Biocytin-soaked gelfoam was applied at the brainstem level at 1 wpi and 3 hours prior to
385 collecting SC tissues. In addition to Biocytin, *syt11b* HCR *in situ* hybridization and HuC/D staining
386 were performed for simultaneous labeling of iNeurons and total neurons, respectively (Fig. 7A).
387 We found that 28-33% of HuC/D$^+$ neurons between 450 and 750 μm caudal to the lesion were
388 labeled (Fig. 7B), indicating integration of caudal neurons into the spinal circuitry as early as 1
389 wpi. 20-38% of rostrally-labeled caudal neurons (Biocytin$^+$ HuC/D$^+$) expressed *syt11b* (Biocytin$^+$
390 HuC/D$^+$ *syt11b*$^+$) (Fig. 7C), suggesting *syt11b*$^+$ iNeurons are part of the integrated SC circuitry at
391 1wpi. To validate these results, we also applied a Biocytin-soaked gelfoam caudal to the lesion at
392 1 wpi and collected SC tissues for histology 3 hours post-labeling (Fig. S7A). Caudal tracing
393 labeled 18-20% of HuC/D$^+$ neurons 450 and 750 μm rostral to the lesion (Biocytin$^+$ HuC/D$^+$) (Fig.
394 S7B), with ~40% of these neurons expressing *syt11b* (Biocytin$^+$ HuC/D$^+$ *syt11b*$^+$) (Fig. S7C).
395 These studies confirmed that iNeurons establish functional connections into the regenerating SC
396 circuitry as early as 1 wpi.

397 **iNeuron genes are required for cellular and functional recovery after spinal cord injury.**
398 To evaluate the roles of iNeuron marker genes during SC regeneration, we employed
399 CRISPR/Cas9 mutagenesis, SCI and functional swim assays (Fig. 7D) (Burris *et al.*, 2021; Klatt
400 Shaw and Mokalled, 2021). Among the top DE markers of N20 iNeurons, 10 genes were filtered
401 as enriched in iNeurons and chosen for mutagenesis (*hdac10, mthfd1l, si:ch211-153j24.3, fhdc5,*
402 *shootin3, syt11b, fam171b, chrnb2b, fblim1, vamp4*) (Fig. S7D). *atf3* was selected as a positive
403 control (Wang *et al.*, 2017). In addition to targeting *syt11b*, we individually and combinatorially
404 targeted the *syt11a* and *syt11b* paralogs to account for putatively redundant effects on
405 regeneration. For efficient and simultaneous gene targeting in zebrafish, we used a recently
406 adapted CRISPR/Cas9 protocol that achieves near complete mutagenesis in F0 injected adults
407 (Burris *et al.*, 2021; Klatt Shaw and Mokalled, 2021). CRISPR/Cas9 targeted animals (crispants)
408 were raised to adulthood and mutagenesis rates were examined by capillary electrophoresis (Fig.
409 S7E). Adult crispants with >90% mutagenesis were subjected to SCI, and swam against
410 increasing water current inside an enclosed swim tunnel to screen for functional regeneration
411 defects. At 4 wpi, swim endurance was significantly reduced in *atf3* and *vamp4* crispants (Fig.
412 7E). Targeting *syt11a and syt11b* paralogs individually did not alter swim endurance. However,
413 swim endurance was diminished in *syt11a;syt11b* dual crispants, indicating the *syt11* paralogs
414 were functionally redundant during SC repair (Fig. 7E). Importantly, overall growth and behavior

415 were comparable between crispant fish and their control siblings prior to SCI, indicating the swim
416 defects observed in these crispants and injury-induced. To validate swim capacity defects in
417 iNeuron gene crispants, we tracked the swim behavior of *atf3*, *vamp4* and *syt11a;syt11b* crispants
418 under at 0, 10 and 20 10 cm/sec current velocities (Fig. 7F). Compared to uninjected control
419 siblings and in the absence of water flow, swim distance was 50-55% reduced in *atf3* and
420 *syt11a;syt11b* crispants and 25% reduced in *vamp4* crispants (Fig. 7F). Swim distance was
421 significantly lower in *atf3*, *vamp4* and *syt11a/b* at 10 and 20 cm/sec water current velocities (Fig.
422 7F). These results indicated the iNeuron markers *atf3*, *vamp4* and *syt11a/b* are required for
423 functional SC repair in zebrafish.
424
425 To date, cellular growth across the lesion has served as a primary readout of cellular
426 regeneration in zebrafish. Glial bridging and axon tracing assays were performed to evaluate the
427 extents of glial and axonal regeneration in iNeuron gene crispants. By Gfap immunostaining, the
428 cross-sectional area of glial bridges was 65% reduced in *atf3* cripants at 4 wpi, but was not
429 significantly affected in *vamp4* and *syt11a;syt11b* crispants compared to controls (Fig. 7G). At this
430 time point, anterograde axon tracing using Biocytin showed comparable axon regrowth from
431 hindbrain neurons into the proximal and distal SC sections between *vamp4*, *syt11a;syt11b* and
432 control animals (Fig. 7H). Consistent with their defective glial bridging, axon regrowth into the
433 proximal and distal sections of caudal SC tissues was markedly impaired in *atf3* cripants. Thus,
434 *vamp4* and *syt11a/b* are required for functional SC repair but dispensable for cellular regeneration
435 across the lesion.

436 These studies showed iNeurons play essential regeneration-independent plasticity-based
437 roles after SCI, and indicated vesicular trafficking is required for the recovery of local neuronal
438 circuitry during innate SC repair.

439 DISCUSSION

440 This study presents a single-cell atlas of innate SC repair in adult zebrafish, uncovers neurons as
441 potent signaling hubs after SCI, identifies cooperative modes of regeneration- and plasticity-
442 based neuronal repair, and shows essential roles for vesicular trafficking in spontaneous neuronal
443 plasticity.

444 The single-cell dataset generated in this study offers a comprehensive resource to determine
445 regenerative cell identities and mechanisms in highly regenerative vertebrates. The use of
446 snRNA-seq is ideal to profile the majority of spinal cell types in zebrafish. Single-cell RNA
447 sequencing is inherently biased against larger cell types such as neurons and astrocytes (Bakken
448 et al., 2018; Lake et al., 2017; Wu et al., 2019). snRNA-seq reduces the challenges of cell
449 dissociation, retrieving large numbers of neurons and glia. While dissection- and dissociation-
450 induced gene expression changes in control samples present a longstanding difficulty for tissue
451 regeneration studies, our protocol minimizes background activation of injury-induced genes by
452 flash-freezing SC tissues from individual animals during tissue collection. Finally, large numbers
453 of nuclei were obtained by pooling frozen SC tissues, minimizing confounding problems
454 associated with snRNA-seq and allowing us to identify small cell populations (Bakken *et al.*, 2018;
455 Ding et al., 2020; Lacar et al., 2016; Lake *et al.*, 2017; van den Brink et al., 2017). Overall, this
456 dataset faithfully represents the proportions and dynamics of major cell populations during
457 zebrafish SC regeneration.

458 Candidate approaches have unveiled central roles for several signaling pathways during SC
459 regeneration (Cavone *et al.*, 2021; Dias et al., 2012; Goldshmit *et al.*, 2012; Reimer et al., 2009;
460 Zhang et al., 2018). Yet, an integrated assessment of regenerative signaling pathways and global
461 assessment of cell-cell interactions were missing. Using CellChat analysis, our single-cell dataset
462 identified a myriad of cell-specific and injury-induced signaling pathways (Jin *et al.*, 2021).
463 Notably, comprehensive assessment of cell-cell signaling networks uncovered neurons as potent
464 sources of signaling in homeostatic and lesioned SC tissues. Injury-induced neuronal signaling
465 pathways include developmental pathways like FGF and WNT, extracellular matrix components
466 like FN1, and axon guidance molecules like SEMA. Concerted activation of these injury-induced
467 pathways is instrumental for neuron survival, neurogenesis, axon regrowth, proper axon guidance
468 and synapse targeting (Briona *et al.*, 2015; Garcia *et al.*, 2018; Goldshmit *et al.*, 2012; He *et al.*,
469 2018; Saraswathy *et al.*, 2022; Tome *et al.*, 2023; Wehner et al., 2017). Further studies of injury-
470 induced signaling pathways will shed light into signaling pathways that direct regeneration- or
471 plasticity-driven SC repair.

472 SC tissues in adult zebrafish retain potent progenitor cells with radial glial features and
473 established contribution to neurogenesis after SCI (Briona *et al.*, 2015; Reimer *et al.*, 2008;
474 Saraswathy *et al.*, 2022). SC regeneration is marked by early imbalance and late restoration of
475 baseline E/I activity. Our data support a model in which excitatory neurons expand and repopulate

476 regenerate SC tissues, while slower and continued neurogenesis of inhibitory neurons underlie
477 the recovery of E/I balance at 6 wpi. These findings are consistent with published studies using a
478 two-cut SCI model in adult zebrafish (Huang *et al.*, 2021), and with the observation that
479 *gad1b*:GFP and *vglut2a*:RFP expression domains are mutually exclusive in our SC sections.
480 Genetic lineage tracing showed excitatory to inhibitory neurotransmitter switching has adverse
481 effects on functional recovery after adult mouse SCI (Bertels *et al.*, 2022). In zebrafish, fast motor
482 neurons were shown to upregulate glutamate expression after injury or exercise (Bertuzzi et al.,
483 2018). Although we cannot rule out similar mechanisms taking place during regeneration, we
484 found that staggered increase in the profiles of newly generated excitatory and inhibitory neurons
485 account for the recovery of E/I balance after SCI. We propose that in depth molecular evaluation
486 of spinal progenitors is needed to better understand the potency and neurogenic capacities of
487 neuronal progenitors during SC regeneration.

488 While zebrafish is an established model of neuron regeneration, our study establishes
489 zebrafish as a renewed model to understand and manipulate fundamental mechanisms of
490 plasticity-based neuronal repair. Neurogenesis-based neural repair is thought to be unattainable
491 in mammals. Instead, the mammalian SCI field has directed its efforts to develop plasticity-based
492 repair strategies. We propose that pre-existing zebrafish neurons upregulate an iNeuron
493 transcriptional signature that includes regeneration associated genes, and that iNeurons elicit
494 spontaneous plasticity during early stages of SC repair. The emergence of iNeurons after SCI is
495 consistent with a recently identified population of embryonically derived dormant neurons that
496 immediately respond to SCI in larval and adult zebrafish (Vandestadt *et al.*, 2021). Similarity to
497 the dormant precursor neurons reported by Vandestadt *et al.,* more than 90% of iNeurons are not
498 newly generated. At 1 wpi, iNeuron signaling accounts for the majority of total neuronal signaling,
499 eliciting particularly strong interactions with OPCs. We propose that future zebrafish studies will
500 contribute insights and applications into mechanisms of plasticity-driven neural repair.

501 Unbiased characterization of the molecular players that direct iNeuron functions after SCI
502 showed multiple components of vesicular trafficking are required for functional SC repair in
503 zebrafish. Syt11a/b (synaptotagmin XI a/b) and Vamp4 (vesicle-associate membrane protein 4)
504 are vesicle-associated proteins that play different roles in neuronal synapses. Syt11 is a non-
505 canonical SNARE that inhibits spontaneous neurotransmission and bulk endocytosis, whereas
506 Vamp4 promotes Calcium-dependent excitatory neurotransmission release and bulk endocytosis
507 (Bakr et al., 2021; Li et al., 2021; Lin et al., 2020; Nicholson-Fish et al., 2015; Shimojo et al., 2019;

508 Wang et al., 2016). Our CRISPR/Cas9 studies showed *syt11a/b* and *vamp4* are required for the
509 recovery of swim function after SCI in zebrafish. These findings are consistent with recent
510 mammalian studies showing that inhibition of the presynaptic release machinery is important for
511 axon regrowth (Hilton et al., 2022), and that *Syt11* knockout in excitatory forebrain neurons
512 impairs synaptic plasticity and memory (Shimojo *et al.*, 2019). Our data reveals vesicular
513 trafficking is an essential mechanism that underlies spontaneous plasticity and rapid neurite
514 outgrowth in iNeurons. We propose that zebrafish provide a valuable model to investigate the
515 origin of iNeurons, elucidate the role of vesicular trafficking in spontaneous plasticity, and identify
516 new manipulations to promote plasticity after SCI.

ACKNOWLEDGMENTS

We thank S. Ackerman, V. Cavalli and A. Johnson for discussion and the Washington University Zebrafish Shared Resource for animal care. We thank S. Nandagopal and T. Tsai for sharing the HCR probe design script. This research was supported by grants from the NIH (R01 NS113915 to M.H.M.) and a Postdoctoral Fellow Seed of Independence Grant from the Department of Developmental Biology at Washington University School of Medicine (to V.M.S.).

ETHICS DECLARATIONS

The authors declare no competing interests.

525 **MATERIAL AND METHODS**

526 **Zebrafish**

527 Adult zebrafish of the Ekkwill, Tubingen and AB strains were maintained at the Washington
528 University Zebrafish Core Facility. All animal experiments were performed in compliance with
529 institutional animal protocols. Size matched (~2 cm) male and female animals of ~4 months of
530 age were used. SC transection surgeries and regeneration analyses were performed in a blinded
531 manner. For all experiments, 2 to 4 independent experimental replicates were performed using
532 different clutches of animals. Within each experiment, experimental fish and control siblings of
533 similar size and equal sex distribution were used. Transected animals from control and
534 experimental groups were housed in equal numbers (4-7 fish) in 1.1-liter tanks. The following
535 previously published zebrafish trains were used: Tg(*vglut2a*:RFP) and Tg(*gad1b*:GFP) (Satou *et*
536 *al.*, 2013).

537 **Spinal cord transection**

538 Complete SC transections were performed as previously described (Mokalled *et al.*, 2016).
539 Briefly, zebrafish were anaesthetized in 0.2 g/L of MS-222 buffered to pH 7.0. Fine scissors were
540 used to make a small incision that transects the SC 4 mm caudal to the brainstem region.
541 Complete transection of the SC was visually confirmed at the time of surgery. Injured animals
542 were also assessed at 2 or 3 dpi to confirm loss of swim capacity post-surgery.

543 **Isolation of spinal cord nuclei from adult zebrafish**

544 For nuclear isolation, a previously described method to isolate nuclei from mouse SC tissues was
545 adapted to zebrafish SCs (Matson *et al.*, 2018). Three mm SC tissue, flanking the lesion site were
546 collected from 50 adult zebrafish at time points 1, 3 and 6 wpi. Corresponding segments of 3 mm
547 SC tissue were collected from uninjured control animals. For tissue lysis, the detergent
548 mechanical lysis protocol described by Matson et al. 2018 was performed. SC tissues were
549 homogenized at low setting for 15 seconds. Density gradient separation using sucrose solution
550 was used to sediment the nuclei from the supernatant. Final nuclear lysates were resuspended
551 using 100 µl of resuspension solution (1x PBS + 2% BSA + 0.2U/µl RNase inhibitor - New England
552 Biolabs, Cat#: M0314S). Hoechst staining was performed to assess the quality of isolated nuclei
553 based on their shape. Samples in which more than 70% of the nuclei were scored as 'healthy'
554 and submitted for single nuclear RNA sequencing.

555 **Single nuclear RNA sequencing**

556 For snRNA-seq, 30 µl of resuspension solution containing isolated nuclei at a concentration of
557 ~1000 nuclei/µl was submitted to Genome Technology Access Center at McDonnel Genome
558 Institute of Washington University. Two biological replicates of each time points at 0, 1, 3 and 6
559 wpi were used. cDNA was prepared after the GEM generation and barcoding, followed by the
560 GEM-RT reaction and bead cleanup steps. cDNA was amplified for 11-13 cycles then purified
561 using SPRIselect beads. Purified cDNA samples were then run on a Bioanalyzer to determine the
562 cDNA concentration. GEX libraries were prepared as recommended by the 10x Genomics
563 Chromium Single Cell 3' Reagent Kits User Guide (v3.1 Chemistry Dual Index) with appropriate
564 modifications to the PCR cycles based on the calculated cDNA concentration. For sample
565 preparation on the 10x Genomics platform, the Chromium Next GEM Single Cell 3' Kit v3.1, 16
566 rxns (PN-1000268), Chromium Next GEM Chip G Single Cell Kit, 48 rxns (PN-1000120), and Dual
567 Index Kit TT Set A, 96 rxns (PN-1000215) were used. The concentration of each library was
568 accurately determined through qPCR utilizing the KAPA library Quantification Kit according to the
569 manufacturer's protocol (KAPA Biosystems/Roche) to produce cluster counts appropriate for the
570 Illumina NovaSeq6000 instrument. Normalized libraries were sequenced on a NovaSeq6000 S4
571 Flow Cell using the XP workflow and a 50x10x16x150 sequencing recipe according to
572 manufacturer protocol. A median sequencing depth of 50,000 reads/cell was targeted for each
573 Gene Expression Library.

574 **Aligning snRNA-seq reads**

575 After sequencing, the Illumina output was processed using the CellRanger (v6.0.0) recommended
576 pipeline to generate gene-barcode count matrices. A custom reference genome was made with
577 the "cellranger mkref" command, using the fasta file of zebrafish reference genome GRCz11
578 constructed from the Ensemble genome build (https://useast.ensembl.org/Danio_rerio/Info/Index)
579 and the sorted Gene Transfer Format file (v4.3.2) from the improved zebrafish transcriptome
580 annotation (Lawson *et al.*, 2020). Base call files for each sample from Illumina were demultiplexed
581 into FASTQ reads. Then, the "cellranger count" pipeline was used to align sequencing reads in
582 FASTQ files to the custom reference genome. Both exon and intron sequences were included
583 during the alignment. The filtered gene-barcode count matrices generated by "cellranger count"
584 was used for downstream analysis.

585 **Quality Control**

586 DecontX package (Yang *et al.*, 2020) (celda v1.16.1) was used to remove droplets containing
587 aberrant counts of ambient mRNA. The function "decontx" was used on the raw "RNA" counts to

588 obtain “decontX” count data. Contamination score was assigned to each cell after running
589 “decontx”. Cells with contamination score greater than 0.75 were filtered out and only “clean” cells
590 (contamination score less than 0.75) were included for downstream analysis. Furthermore,
591 decontX counts were used as default for pre-processing and normalization. After ambient RNA
592 removal, DoubletFinder (McGinnis *et al.*, 2019) (v2.0.3) was used to identify doublets formed from
593 transcriptionally distinct cells. Optimal pK values were calculated from the outputs of function
594 “paramsweep_v3”. Then, “doubletFinder_v3” function was used to predict doublet cells, where 50
595 principal components and pN value of 0.25 were given as input along with the previously
596 calculated pK values (0.26). All the cells predicted as doublets were removed.

597 **Integrated analysis of snRNA-seq dataset**

598 All the datasets were integrated and analyzed using Seurat (v4.1.1) package with R (v4.2.1) (R
599 Core Team, 2018; Stuart et al., 2019). Each sample count matrix was filtered for genes that were
600 expressed in at least 3 cells and cells expressing at least 200 genes, followed by cell quality
601 assessment using commonly used QC matrixes (Ilicic et al., 2016). Cells having a unique number
602 of genes between 200 to 4000 and a mitochondrial gene percentage <5 were used for
603 downstream processing. Each dataset was independently normalized and scaled using the
604 “SCTransform” function, which is an improved method for normalization, that performs a variance-
605 stabilizing transformation using negative binomial regression (Hafemeister and Satija, 2019).
606 Standard integration workflow of Seurat was used to identify shared sources of variation across
607 experiments as well as mutual nearest neighbors (Butler et al., 2018; Haghverdi et al., 2018).
608 Integration features were selected based on the top 4000 highly variable features using
609 “SelectIntegrationFeatures” function (nfeatures = 4000), which was used as input for the
610 “anchor.features” argument of the “FindIntegrationAnchors” function. PCA analysis was
611 performed on the 4000 variable features and the top 50 principal components selected based on
612 the elbow plot heuristic, which measures the contribution of variation in each component. These
613 50 principal components were used in “FindNeighbors” and “FindClusters” functions to perform
614 graph-based clustering on a shared nearest neighbor graph (Levine et al., 2015; Xu and Su,
615 2015). Louvain algorithm was used for modularity optimization in clustering the cells using
616 “FindClusters” function. The resolution parameter (res = 0.4) that determines the granularity of
617 the clustering was selected by visually inspecting clusters with resolutions ranging 0.1 - 2.0 as
618 well as clustree graphs (Zappia and Oshlack, 2018). Uniform Manifold Approximation and
619 Reduction (UMAP) was used for non-linear dimensional reduction of the first 50 principal
620 components and visualize the data using “RunUMAP” function (Becht et al., 2018). Data was

621 graphed using different plot functions, such as “DimPlot”, “VlnPlot”, “FeaturePlot”, “Dotplot” and
622 “DoHeatmap”, to view the cell cluster identity and marker gene expression. Cell proportion data
623 was extracted using “table” and “prop.table” functions. Differential gene expression for individual
624 cluster was identified using Wilcoxon rank sum test in the “FindAllMarkers” function. Marker genes
625 detected in at least 25% of the clustered cells and with a logFC threshold of 0.25 were selected.
626 Only positive markers were reported.

627 **Subset analysis of neuron clusters**

628 The neuron cell clusters identified from the complete dataset were subclustered using the “subset”
629 function for subcluster analysis. The subset was again normalized and scaled using
630 “SCTransform” function with glmGamPoi method (Ahlmann-Eltze and Huber, 2021). Fifty principal
631 components were used, and the resolution parameter was set to 0.6. Further downstream
632 analysis was done as described above for the integrated analysis. The top DE markers generated
633 for each neuron subcluster using “FindAllMarkers” function is given in table S4.

634 **Cluster identification using differentially expressed markers.**

635 A “CNS markers” database of previously published markers of the different cell types that
636 comprise the vertebrate brain and/or SC tissues was compiled (Baek *et al.*, 2019; Cavone *et al.*,
637 2021; Guillemot, 2007; Haring *et al.*, 2018; Hayashi *et al.*, 2018; Hernandez-Miranda *et al.*, 2017;
638 Lu *et al.*, 2015; Milich *et al.*, 2021; Rosenberg *et al.*, 2018; Rougeot *et al.*, 2019; Sathyamurthy *et*
639 *al.*, 2018; Tambalo *et al.*, 2020; Tang *et al.*, 2017; Yadav *et al.*, 2023; Zeisel *et al.*, 2018; Zhang
640 *et al.*, 2014). For each cell cluster, every marker gene identified as a top differentially expressed
641 (DE) marker of that cluster was cross-referenced with our compiled “CNS markers” database
642 (Table S1), using our “DEMarkerScoring” algorithm. For every matching marker gene, one point
643 was given to the respective cluster under the column name with the matching cell identity. Iteration
644 over every marker gene was performed to generate a scoring matrix with varying points for each
645 cluster against the different cell identities compiled in the “CNS markers” database (Table S2,
646 sheet: scoring). Then, “phyper” function in R was used to calculate binomial probabilities using
647 hypergeometric distribution for the total score obtained by each cluster against each cell identity
648 in the database (Table S2, sheet: Binomial probability). Then, -log10 of probability values are
649 obtained for plotting the heatmap (Table S2, sheet: -log10P). The resulting values were scaled to
650 0-100 and plotted as a heatmap using GraphPad prism. Each cluster was given an identity based
651 on the maximum -log10 P score obtained in the heatmap. The top DE markers of clusters with
652 ambiguous scores are manually searched in the literature (Zhang *et al.*, 2014; Zhang et al., 2016)

653 (https://brainrnaseq.org/) to confirm cluster identity. “RenameIdents” function was used to assign
654 identity to each cluster. For confirmation of the assigned cluster identity, enrichment of classical
655 markers of respective cell types were tested using Dot plot. The “DEMarkerScoring” algorithm is
656 available here:
657 https://github.com/MokalledLab/Zebrafish_SCI_Atlas/blob/main/s7_marker_comparison_v3.R .

658 **Filtering differentially expressed markers for candidate gene selection.**
659 To identify candidate genes that are uniquely expressed in N20 iNeurons, top DE markers were
660 cross-checked and filtered against the top DE markers of all the other neuron subclusters.
661 Enrichment and percent expression of these unique genes were then confirmed using Dot plots.
662 Genes that were enriched or expressed in other neuronal or non-neuronal subclusters, in addition
663 to their expression in iNeurons, were omitted. Genes that are exclusively enriched in iNeurons
664 were selected for generating crispants.

665 **Cell-cell interaction assay**
666 The R package CellChat (v1.4.0) was used to evaluate regenerative cell-cell interactions after
667 SCI (Jin *et al.*, 2021). CellChat models the probability of cell-cell communication by integrating
668 our gene expression data with a database (CellChatDB) of known interaction between signaling
669 ligands, receptors, and their cofactors. CellChatDB is a manually curated from literature-
670 supported ligand-receptor interactions in human and mouse, only. Therefore, we converted the
671 normalized RNA data matrix of our zebrafish dataset at each time point into human orthologues
672 using Ensemble biomaRT package (Durinck et al., 2009). The following rules were applied while
673 converting the data matrix: 1) one-to-one orthologue mapping was performed whenever possible,
674 2) For genes with one to several human orthologues, the corresponding zebrafish RNA data value
675 was copied to every mapped gene in humans, 3) RNA data values were eliminated for zebrafish
676 genes that did not have any human orthologue, 4) RNA data values of paralogous zebrafish genes
677 were added and the cumulative data value was assigned to the human orthologue
678 (https://github.com/MokalledLab/Zebrafish_SCI_Atlas/blob/main/Sparse_matrix_homologe_con
679 verter_082322.R) . The converted RNA data was used then to create CellChat object using
680 “createCellChat” function, followed by the recommended preprocessing functions with default
681 parameters for the analysis of individual datasets. Truncated mean method with 10% trimmed
682 observation was used to compute average gene expression per cell group in for the complete
683 dataset (Fig. 2 and S2). The default trimean method was used to compute average gene
684 expression for the CellChat analysis of neuron subset (Fig. 5 and S5). CellChatDB.human was

685 used as the database for inferring cell-cell communication. All categories of ligand-receptor
686 interactions in the database were used in the analysis. Communications involving less than 10
687 cells were excluded. Function “netAnalysis_computeCentrality” was used to calculate network
688 centrality scores at each time point. Functions such as “netVisual_circle”,
689 “netAnalysis_contribution”, “netVisual_aggregate”, “netVisual_bubble” and
690 “netAnalysis_signalingRole_heatmap” were used to generate different plots used in this paper.

691 **Trajectory inference analysis**

692 Pseudotime analysis was performed using CellRank (v1.5.1) package in Python (v3.8.10) (Lange
693 et al., 2022; Rossum and Drake, 2009). Before analysis, the Seurat object was converted to an
694 AnnData in a two-step process using the R package SeuratDisk (v0.9020). First, the Seurat object
695 was saved as an h5Seurat file and then, converted it to an AnnData file to use as an input for
696 pseudotime analysis using CellRank. Basic pre-processing of the AnnData file was performed
697 with default recommended settings using the scvelo (v0.2.4) and scanpy (v1.9.1) packages.
698 Genes expressed in at least 10 cells were included and 30 principal components and neighbors
699 were used for preprocessing of the data. CytoTRACEkernel was used for pseudotime
700 computation and direct KNN graph-edges to point into the direction of increasing differentiation
701 status (Gulati *et al.*, 2020). The transition matrix was calculated by setting the threshold_scheme
702 parameter to “soft” to reconstruct cellular trajectories using VIA algorithm (Stassen et al., 2021).
703 This transition matrix was projected onto a UMAP plot to obtain a velocity graph.

704 **Gene ontology**

705 Gene ontology analysis was performed using Metascape (Zhou et al., 2019). Input and analysis
706 species were set as D. rerio. Express analysis was performed for gene ontology. Metascape
707 identified all statistically enriched terms (including GO biological processes, Reactome gene set
708 and KEGG pathway), and calculated accumulative hypergeometric p-values and enrichment
709 factors. Significant terms were hierarchically clustered into a tree based on Kappa-statistical
710 similarities among their gene memberships. A kappa score of 0.3 was applied to cast the tree into
711 term clusters. The most enriched term in each cluster was chosen as the representative term.

712 **Regeneration Score**

713 Genes associated with the GO term “regeneration” in the database Amigo
714 (http://amigo.geneontology.org/amigo/landing) were identified. As a result, Regeneration
715 Associated Genes (RAG) present in the following terms were included: axon extension involved

716 in regeneration_GO_0048677, Axon regeneration_GO_0031103, dendrite
717 regeneration_GO_0031104, Positive regulation of axon regeneration_GO_0048680, Positive
718 regulation of neuron projection regeneration_GO_0070572, Regeneration_GO_0031099 (Table
719 S5). Regeneration score for each neuron cluster was calculated based on the DE expressed
720 markers obtained through "FindAllMarkers" function. All upregulated marker genes detected in at
721 least 25% of the clustered cells and with a logFC threshold of 0.25 were considered top DE
722 markers. Our previously mentioned "DEMarkerScoring" algorithm was then used to cross-
723 reference and score each cluster based on the similarity between Top DE markers and RAG. -
724 log10P value was used to generate the UMAP plot with the regeneration score. Raw values are
725 detailed given in Table S4 (sheet Cluster ID).

726 **Histology**

727 Sixteen µm cross cryosections of paraformaldehyde fixed SC tissues were used. Tissue sections
728 were mainly imaged using a Zeiss LSM 800 confocal microscope (Axio Imager.Z2, Objective:
729 Plan-Apochromat 20x/0.8 M27, Detector: Multialkali-PMT) for immunofluorescence and
730 hybridization chain reaction (HCR) RNA *in situ* hybridization. For glial bridging and axon-regrowth
731 assay (Fig. 8D, F), images were taken using Zeiss slide scanner (Axio Scan.Z1, Objective: Plan-
732 Apochromat 20x/0.8 M27, Imaging device: OrcaFlash)

733 The HCR RNA *in situ* hybridization protocol was adapted from Molecular Instruments
734 (https://www.molecularinstruments.com/hcr-ihc-protocols) (Choi et al., 2018). Briefly, tissue
735 sections were hydrated in PBS, dehydrated stepwise into 100% ethanol, then rehydrated stepwise
736 into PBT (0.1% Tween-20 in PBS). Sections were pre-treated either with 0.2% TritonX-100 in
737 PBS for 5 minutes or boiled in Citrate Buffer (10mM Citric Acid, 0.05% Tween-20, pH 6.0) for 10
738 minutes. For blocking, sections were incubated in Hybridization buffer (Molecular Instruments) for
739 1 hr at 37°C. For hybridization, sections were incubated in pre-warmed DNA probe sets diluted to
740 0.0015 pmol/uL in Hybridization buffer for 48 hrs at 37°C. Washes were then performed with Wash
741 Buffer (Molecular Instruments) at 37°C followed by 5x SSCT (3M NaCl, 0.3 M Sodium Citrate,
742 0.1% Tween-20, pH 7.0). For signal amplification, sections were incubated in Amplification buffer
743 (Molecular Instruments) for 1 hr at room temperature. Prior to amplification, h1 and h2 hairpins
744 were snap-cooled in individual tubes by heating to 95°C and allowing tubes to return to ambient
745 temperature slowly. For amplification, h1 and h2 snap-cooled hairpins were mixed together and
746 diluted 1:50 in Amplification buffer. Amplification proceeded overnight at room temperature in the
747 dark. Samples were then washed thoroughly in 5x SSCT, 5x SSC, and PBT at room temperature

748 before proceeding to immunohistochemistry. HCR RNA probes used in this study (*syt11a, syt11b,*
749 and *vamp4*) were designed using a python script. Probe sets were ordered as 50 pmol opools
750 from IDT. Oligo sequences for each probe set are provided in Table S7.

751 For immunohistochemistry, tissue sections were hydrated in PBT then treated with blocking agent
752 (5% goat serum in PBT) for 1 hr at room temperature. For nuclear antigens, sections were treated
753 with 0.2% TritonX-100 in PBT for 5 minutes and washed thoroughly in PBT prior to the blocking
754 step. Sections were incubated overnight at 4°C with respective primary antibodies diluted in
755 blocking agent, then washed in PBT, and treated for 1 hour in secondary antibodies diluted in
756 blocking agent at room temperature. For EdU staining, sections are incubated with freshly
757 prepared EdU staining solution (100mM Tris at pH 8.5 - SIGMA T6066, 1 mM $CuSO_4$ – SIGMA
758 C1297, 200 µM Fluorescent azide – Thermo Fischer Scientific and 100 mM Ascorbic Acid -
759 SIGMA A5960) for 30 minutes in the dark at room temperature (Salic and Mitchison, 2008).
760 Following washes, sections were incubated in 1 µg/mL of Hoechst (Thermo Scientific, H3570) for
761 3 minutes, washed in PBT and mounted in Fluoromount-G mounting media (SouthernBiotech,
762 0100-01). Primary antibodies used in this study were chicken anti-GFP (AVES, 1020, 1:1000),
763 rabbit anti-dsRed (Clontech, 632496, 1:250), mouse anti-HuC/D (Invitrogen, A21271, 1:500).
764 Secondary antibodies (Invitrogen, 1:250) used in this study were Alexa Flour 488, Alexa Flour
765 594, and Alexa Flour 647 goat anti-rabbit or goat anti-mouse antibodies.

766 **Rostral and caudal axon tracing**

767 Two sets of axon tracing experiments were performed at 1 wpi (Mokalled *et al.*, 2016). For rostral
768 labeling, fish were anaesthetized using MS-222 and fine scissors were used to transect the cord
769 4 mm rostral to the lesion site. For caudal labeling, fish were anaesthetized using MS-222 and
770 fine scissors were used to transect the cord 4 mm caudal to the lesion site. For both sets of tracing
771 experiments, Biocytin-soaked Gelfoam Gelatin Sponge was applied at the new injury site
772 (Gelfoam, Pfizer, cat# 09-0315-08; Biocytin, saturated solution, Sigma, Cat# B4261). Fish were
773 euthanized 3 hours post-treatment and Biocytin was histologically detected using Alexa Fluor
774 594-conjugated Streptavidin (Thermo Fisher, cat# S-11227). *syt11b* HCR in situ hybridization and
775 HuC/D staining were performed on the same sections. The numbers of Biocytin$^+$ HuC/D$^+$ and
776 Biocytin$^+$ HuC/D$^+$ *syt11b*$^+$ neurons were calculated 150, 450, and 750 µm rostral and caudal to
777 the lesion. The numbers of Biocytin$^+$ HuC/D$^+$ were normalized to HuC/D$^+$ neurons to estimate the
778 extent of labeling. The numbers of Biocytin$^+$ HuC/D$^+$ *syt11b*$^+$ neurons were then normalized to
779 Biocytin$^+$ HuC/D$^+$ neurons to estimate the extent of iNeuron integration in the labeled circuitry. We

780 note that in the axon tracing experiments performed at 1 wpi (Figure 7 and S7), we observed
781 ectopic Biocytin labelling of ependymal glial cells on the non-labeled side of the cord distal to the
782 lesion site (caudal ependymal glial cells distal to the lesion were Biocytin$^+$ following rostral tracing;
783 rostral ependymal glial cells distal to the lesion were Biocytin$^+$ following caudal tracing). This
784 labeling is not usually observed by axon tracing at 4 or 6 wpi.

785 **CRISPR/Cas9 mutagenesis**

786 CRISPR/Cas9 design, mutagenesis and screening was performed as previously described (Klatt
787 Shaw and Mokalled, 2021). Briefly, crRNA guide RNA sequences were selected using
788 CHOPCHOP (https://chopchop.cbu.uib.no/). Only sequences with no off-target sites with three or
789 fewer mismatches elsewhere in the genome were selected. To maximize the effect of small indels,
790 target sites were chosen that lie within essential domains (Table S5). Alt-R tracrRNA and crRNA
791 gRNAs (IDT, Cat# 1072534) were reconstituted using manufacturer's specifications as 100 μM
792 stocks, then annealed at a final concentration of 50 μM. Alt-R S.p. Cas9 nuclease V3 (IDT, Cat#
793 1081059) was diluted in Cas9 dilution buffer (1 M HEPES at pH 7.5, 2 M KCl) to a working
794 concentration of 25 μM. Annealed dgRNA duplexes were diluted 1:1 in duplex buffer (IDT, Cat#
795 11-05-01-03) to a working concentration of 25 μM. Equal volumes of dgRNA were added to Cas9
796 protein and incubated at 37°C for 5 minutes. For dual targeting of *syt11a* and *syt11b*, Cas9 protein
797 was added in equal molar amounts to the total concentration of dgRNA. Tubingen wild-type
798 embryos were injected with 1 nL of CRISPR/Cas9 solution at the one-cell stage and grown to
799 adulthood for genotyping, SC surgeries and functional analysis. The full sequence for each guide
800 RNAs is provided in Table S6.

801 **Genotyping by capillary electrophoresis**

802 Capillary electrophoresis was used to calculate the indel frequency for each CRISPR/Cas9 target
803 site. For DNA extraction, whole 4 dpf larvae or ~3 mm of excised adult tail fins were added to 20
804 μL (larvae) or 50 μL (adult fin) of fin lysis buffer (10 mM Tris at pH 7.0, 50 mM KCl, 1 mM EDTA
805 at pH 8.0, 0.3% Tween-20, freshly added Proteinase K at 200 μg/ml). DNA samples were
806 incubated at 55°C for 60 minutes and then, followed by a 15-minute incubation at 95°C. 150-250
807 bp PCR products were generated using NEB Taq Polymerase (Cat# M0273) with gene-specific
808 primers (Table S5) in a volume of 10 μL in Pryme PCR semi-skirted PCR plates (MidSci, Cat#
809 AVRT1). Samples were diluted to 24 μL in TE dilution buffer (Agilent, DNF-495-0060) and loaded
810 into the 5200 Fragment Analyzer System (Agilent, Cat# M5310AA). Capillary electrophoresis was

811 carried out using the Agilent Fragment Analyzer Qualitative DNA Kit (Cat# DNF-905-K1000)
812 according to the manufacturer's specifications.

813 To calculate indel frequency, 2 wild-type control siblings were PCR amplified. The size of wild-
814 type products was determined using these control samples. PCR products with peaks within 1 bp
815 of control amplicon size were termed wild types (non-indel). Indel frequency was calculated by
816 dividing the signal intensity of total non-indel peaks by the cumulative intensity of all peaks in each
817 sample. Because of significant noise due to primers (<100 bp) and non-specific products (>300
818 bp) in wild-type samples, only signals between 100 and 300 bp were used to calculate indel
819 frequency.

820 **Swim endurance assay**

821 Swim endurance assays were performed as previously described (Burris *et al.*, 2021). Zebrafish
822 were exercised in groups of 8-15 in a 5 L swim tunnel device (Loligo, Cat# SW100605L,
823 120V/60Hz). After 5 minutes of acclimation (with no flow) inside the enclosed tunnel, fish were
824 swum at 9 cm/s and 10 cm/s for 5 minutes each to evaluate their swimming capability at bare
825 minimum velocity. Water current velocity was then increased every two minutes and fish swam
826 against the current until they reached exhaustion. Exhausted animals were removed from the
827 chamber without disturbing the remaining fish. Swim time at exhaustion was recorded for each
828 fish. Fish that were exhausted before the first 15 minutes were considered poorly recovered.
829 Percent recovery was calculated by dividing the number of fish that swam more than 15 minutes
830 to the total number of fish present in the group.

831 **Swim behavior assay**

832 Swim behavior assays were performed as previously described (Burris *et al.*, 2021). Zebrafish
833 were divided into groups of 5 in a 5 L swim tunnel device (Loligo, Cat# SW100605L, 120V/60Hz).
834 Each group was allowed to swim for a total of 15 min under zero to low current velocities (5 min
835 at 0 cm/s, 5 min at 10 cm/s, and 5 min at 15 cm/s). The entire swim session was recorded using
836 high-speed camera (iDS, USB 3.0 color video camera) with following settings: aspect ratio, 1:4;
837 pixel clock, 344; frame rate, 70 frames/s; exposure time: 0.29; aperture, 1.4 to 2; maximum
838 frames; 63,000. Movies were converted to 20 frames/s and analyzed using a customized Fiji
839 macro
840 (https://github.com/MokalledLab/Zebrafish_SCI_Atlas/blob/main/Swim%20behavior_Tracking_v
841 2.ijm). For each frame, animals/objects >1500 px2 were identified, and the XY coordinates were

842 derived for each animal/object. Each frame was independently analyzed, and animal/object
843 tracking was completed using a customized R Studio script
844 (https://github.com/MokalledLab/Zebrafish_SCI_Atlas/blob/main/SwimBehavior_processing%20
845 and%20quantification_v7.R). The script aligned coordinates, calculated swim metrics considering
846 three separate frame windows (Frames 0-6000 at 0 cm/s; frames 6001-12000 at 10 cm/s, and
847 frames 12001-18001 at 20 cm/s). Distance swam was analyzed at 0, 10, and at 15 cm/s.

848 **Axon regrowth assay**

849 Anterograde axon tracing was performed on adult zebrafish at 28 dpi as previously described
850 (Mokalled *et al.*, 2016). Fish were anaesthetized using MS-222 and fine scissors were used to
851 transect the cord 4 mm rostral to the lesion site. Biocytin-soaked Gelfoam Gelatin Sponge was
852 applied at the new injury site (Gelfoam, Pfizer, cat# 09-0315-08; Biocytin, saturated solution,
853 Sigma, Cat# B4261). Fish were euthanized 3 hours post-treatment and Biocytin was histologically
854 detected using Alexa Fluor 594-conjugated Streptavidin (Thermo Fisher, cat# S-11227). Biocytin-
855 labeled axons were quantified using the "threshold" and "particle analysis" tools in the Fiji
856 software. Four sections per fish at 0.5 (proximal) and 2 (distal) mm caudal to the lesion core, and
857 2 sections 1 mm rostral to the lesion, were analyzed. Axon growth was normalized to the efficiency
858 of Biocytin labeling rostral to the lesion for each fish. The axon growth index was then normalized
859 to the control group for each experiment.

860 **Glial bridging assay**

861 Gfap immunohistochemistry was performed on serial sections. The cross-sectional area of the
862 glial bridge and the area of the intact SC rostral to the lesion were measured using ImageJ
863 software. Bridging was calculated as a ratio of these measurements.

864 **Quantifications**

865 *Cell counting.* Cell counting were performed using a customized Fiji script
866 (adapting ITCN plugin: Image based Tool for counting nuclei -
867 https://github.com/MokalledLab/Zebrafish_SCI_Atlas/blob/main/Cell_Counter_v1-5_vms.ijm).
868 Orthogonal projections of individual image stacks were generated using Zen software. A
869 customized Fiji script incorporated user-defined inputs to define channels (including Hoechst) and
870 to outline SC perimeters. To quantify nuclei, the following parameters were set in ITCN counter:
871 width – 15; minimal distance – 7.5; threshold – 0.4. Once nuclei were identified, user-defined
872 thresholds of individual cell markers were used to mask the image and identify nuclei located

873 inside the masked regions. X/Y coordinates were extracted for each nucleus for cell counting.
874 Raw counts and X/Y coordinates from Fiji were processed using a customized R script
875 (https://github.com/MokalledLab/Zebrafish_SCI_Atlas/blob/main/Cell_Count_Processor_v1_vms
876 .R). Markers that share nuclei with the same X/Y coordinates were considered overlapping.

877 *Quantifying HCR in situ signal.* HCR *in situ* hybridization signals were quantified using a
878 customized Fiji script
879 (https://github.com/MokalledLab/Zebrafish_SCI_Atlas/blob/main/hcr_celltypespecific_analysis_v
880 3.1_080222.ijm). Orthogonal projections of individual image stacks were generated using the Zen
881 software (Zeiss). ROIs around SC borders were defined to exclude non-SC tissues and user-
882 defined thresholds were set to create an inverted mask. Background noise was either manually
883 corrected or defined by thresholding a dedicated, unstained background channel. Integrated
884 density was quantified for fluorescence signals inside the quantification mask using the "Analyze
885 Particles" command. To calculate the HCR *in situ* hybridization signal inside neurons, an inverted
886 mask was created after thresholding HuC/D$^+$ neurons, then added to the final quantification mask.
887 The fluorescence signals inside this newly generated mask were considered neuron specific.

1047 **REFERENCES**

1048 Ahlmann-Eltze, C., and Huber, W. (2021). glmGamPoi: fitting Gamma-Poisson generalized linear
1049 models on single cell count data. Bioinformatics *36*, 5701-5702. 10.1093/bioinformatics/btaa1009.

1050 Anderson, M.A., O'Shea, T.M., Burda, J.E., Ao, Y., Barlatey, S.L., Bernstein, A.M., Kim, J.H.,
1051 James, N.D., Rogers, A., Kato, B., et al. (2018). Required growth facilitators propel axon
1052 regeneration across complete spinal cord injury. Nature *561*, 396-400. 10.1038/s41586-018-
1053 0467-6.

1054 Baek, M., Menon, V., Jessell, T.M., Hantman, A.W., and Dasen, J.S. (2019). Molecular Logic of
1055 Spinocerebellar Tract Neuron Diversity and Connectivity. Cell Rep *27*, 2620-2635 e2624.
1056 10.1016/j.celrep.2019.04.113.

1057 Bakken, T.E., Hodge, R.D., Miller, J.A., Yao, Z., Nguyen, T.N., Aevermann, B., Barkan, E.,
1058 Bertagnolli, D., Casper, T., Dee, N., et al. (2018). Single-nucleus and single-cell transcriptomes
1059 compared in matched cortical cell types. PLoS One *13*, e0209648.
1060 10.1371/journal.pone.0209648.

1061 Bakr, M., Jullie, D., Krapivkina, J., Paget-Blanc, V., Bouit, L., Petersen, J.D., Retailleau, N.,
1062 Breillat, C., Herzog, E., Choquet, D., and Perrais, D. (2021). The vSNAREs VAMP2 and VAMP4
1063 control recycling and intracellular sorting of post-synaptic receptors in neuronal dendrites. Cell
1064 Rep *36*, 109678. 10.1016/j.celrep.2021.109678.

1065 Bartus, K., Burnside, E.R., Galino, J., James, N.D., Bennett, D.L.H., and Bradbury, E.J. (2019).
1066 ErbB receptor signaling directly controls oligodendrocyte progenitor cell transformation and
1067 spontaneous remyelination after spinal cord injury. Glia *67*, 1036-1046. 10.1002/glia.23586.

1068 Becht, E., McInnes, L., Healy, J., Dutertre, C.A., Kwok, I.W.H., Ng, L.G., Ginhoux, F., and Newell,
1069 E.W. (2018). Dimensionality reduction for visualizing single-cell data using UMAP. Nat Biotechnol.
1070 10.1038/nbt.4314.

1071 Bertels, H., Vicente-Ortiz, G., El Kanbi, K., and Takeoka, A. (2022). Neurotransmitter phenotype
1072 switching by spinal excitatory interneurons regulates locomotor recovery after spinal cord injury.
1073 Nat Neurosci *25*, 617-629. 10.1038/s41593-022-01067-9.

1074 Bertuzzi, M., Chang, W., and Ampatzis, K. (2018). Adult spinal motoneurons change their
1075 neurotransmitter phenotype to control locomotion. Proc Natl Acad Sci U S A *115*, E9926-E9933.
1076 10.1073/pnas.1809050115.

1077 Bradbury, E.J., Moon, L.D., Popat, R.J., King, V.R., Bennett, G.S., Patel, P.N., Fawcett, J.W., and
1078 McMahon, S.B. (2002). Chondroitinase ABC promotes functional recovery after spinal cord injury.
1079 Nature *416*, 636-640. 10.1038/416636a.

1080 Brennan, F.H., and Popovich, P.G. (2018). Emerging targets for reprograming the immune
1081 response to promote repair and recovery of function after spinal cord injury. Curr Opin Neurol *31*,
1082 334-344. 10.1097/WCO.0000000000000550.

1083 Briona, L.K., Poulain, F.E., Mosimann, C., and Dorsky, R.I. (2015). Wnt/ss-catenin signaling is
1084 required for radial glial neurogenesis following spinal cord injury. Dev Biol *403*, 15-21.
1085 10.1016/j.ydbio.2015.03.025.

1086 Burris, B., Jensen, N., and Mokalled, M.H. (2021). Assessment of Swim Endurance and Swim
1087 Behavior in Adult Zebrafish. J Vis Exp. 10.3791/63240.

1088 Butler, A., Hoffman, P., Smibert, P., Papalexi, E., and Satija, R. (2018). Integrating single-cell
1089 transcriptomic data across different conditions, technologies, and species. Nat Biotechnol *36*,
1090 411-420. 10.1038/nbt.4096.

1091 Cardozo, M.J., Mysiak, K.S., Becker, T., and Becker, C.G. (2017). Reduce, reuse, recycle -
1092 Developmental signals in spinal cord regeneration. Dev Biol *432*, 53-62.
1093 10.1016/j.ydbio.2017.05.011.

1094 Carulli, D., de Winter, F., and Verhaagen, J. (2021). Semaphorins in Adult Nervous System
1095 Plasticity and Disease. Front Synaptic Neurosci *13*, 672891. 10.3389/fnsyn.2021.672891.

1096 Cavone, L., McCann, T., Drake, L.K., Aguzzi, E.A., Oprisoreanu, A.M., Pedersen, E., Sandi, S.,
1097 Selvarajah, J., Tsarouchas, T.M., Wehner, D., et al. (2021). A unique macrophage subpopulation
1098 signals directly to progenitor cells to promote regenerative neurogenesis in the zebrafish spinal
1099 cord. Dev Cell *56*, 1617-1630 e1616. 10.1016/j.devcel.2021.04.031.

1100 Choi, H.M.T., Schwarzkopf, M., Fornace, M.E., Acharya, A., Artavanis, G., Stegmaier, J., Cunha,
1101 A., and Pierce, N.A. (2018). Third-generation in situ hybridization chain reaction: multiplexed,
1102 quantitative, sensitive, versatile, robust. Development *145*. 10.1242/dev.165753.

1103 Curtis, R., Green, D., Lindsay, R.M., and Wilkin, G.P. (1993). Up-regulation of GAP-43 and growth
1104 of axons in rat spinal cord after compression injury. J Neurocytol *22*, 51-64. 10.1007/BF01183975.

1105 DePaul, M.A., Lin, C.Y., Silver, J., and Lee, Y.S. (2017). Combinatory repair strategy to promote
1106 axon regeneration and functional recovery after chronic spinal cord injury. Sci Rep *7*, 9018.
1107 10.1038/s41598-017-09432-6.

1108 Dias, T.B., Yang, Y.J., Ogai, K., Becker, T., and Becker, C.G. (2012). Notch signaling controls
1109 generation of motor neurons in the lesioned spinal cord of adult zebrafish. J Neurosci *32*, 3245-
1110 3252. 10.1523/JNEUROSCI.6398-11.2012.

1111 Diez Del Corral, R., and Morales, A.V. (2017). The Multiple Roles of FGF Signaling in the
1112 Developing Spinal Cord. Front Cell Dev Biol *5*, 58. 10.3389/fcell.2017.00058.

1113 Ding, J., Adiconis, X., Simmons, S.K., Kowalczyk, M.S., Hession, C.C., Marjanovic, N.D., Hughes,
1114 T.K., Wadsworth, M.H., Burks, T., Nguyen, L.T., et al. (2020). Systematic comparison of single-
1115 cell and single-nucleus RNA-sequencing methods. Nat Biotechnol *38*, 737-746. 10.1038/s41587-
1116 020-0465-8.

1117 Doster, S.K., Lozano, A.M., Aguayo, A.J., and Willard, M.B. (1991). Expression of the growth-
1118 associated protein GAP-43 in adult rat retinal ganglion cells following axon injury. Neuron *6*, 635-
1119 647. 10.1016/0896-6273(91)90066-9.

1120 Dudek, F.E., and Sutula, T.P. (2007). Epileptogenesis in the dentate gyrus: a critical perspective.
1121 Prog Brain Res *163*, 755-773. 10.1016/S0079-6123(07)63041-6.

1122 Durinck, S., Spellman, P.T., Birney, E., and Huber, W. (2009). Mapping identifiers for the
1123 integration of genomic datasets with the R/Bioconductor package biomaRt. Nat Protoc *4*, 1184-
1124 1191. 10.1038/nprot.2009.97.

1125 Fouad, K., Popovich, P.G., Kopp, M.A., and Schwab, J.M. (2021). The neuroanatomical-functional
1126 paradox in spinal cord injury. Nat Rev Neurol *17*, 53-62. 10.1038/s41582-020-00436-x.

1127 Gao, R., and Penzes, P. (2015). Common mechanisms of excitatory and inhibitory imbalance in
1128 schizophrenia and autism spectrum disorders. Curr Mol Med *15*, 146-167.
1129 10.2174/1566524015666150303003028.

1130 Garcia, A.L., Udeh, A., Kalahasty, K., and Hackam, A.S. (2018). A growing field: The regulation
1131 of axonal regeneration by Wnt signaling. Neural Regen Res *13*, 43-52. 10.4103/1673-
1132 5374.224359.

1133 Gey, M., Wanner, R., Schilling, C., Pedro, M.T., Sinske, D., and Knoll, B. (2016). Atf3 mutant mice
1134 show reduced axon regeneration and impaired regeneration-associated gene induction after
1135 peripheral nerve injury. Open Biol *6*. 10.1098/rsob.160091.

1136 Goldshmit, Y., Sztal, T.E., Jusuf, P.R., Hall, T.E., Nguyen-Chi, M., and Currie, P.D. (2012). Fgf-
1137 dependent glial cell bridges facilitate spinal cord regeneration in zebrafish. J Neurosci *32*, 7477-
1138 7492. 10.1523/JNEUROSCI.0758-12.2012.

1139 Guillemot, F. (2007). Spatial and temporal specification of neural fates by transcription factor
1140 codes. Development *134*, 3771-3780. 10.1242/dev.006379.

1141 Gulati, G.S., Sikandar, S.S., Wesche, D.J., Manjunath, A., Bharadwaj, A., Berger, M.J., Ilagan,
1142 F., Kuo, A.H., Hsieh, R.W., Cai, S., et al. (2020). Single-cell transcriptional diversity is a hallmark
1143 of developmental potential. Science *367*, 405-411. 10.1126/science.aax0249.

1144 Guo, X.Y., Duan, F.X., Chen, J., Wang, Y., Wang, R., Shen, L., Qi, Q., Jiang, Z.Q., Zhu, A.Y., Xi,
1145 J., et al. (2019). Subcutaneous Administration of PDGF-AA Improves the Functional Recovery
1146 After Spinal Cord Injury. Front Neurosci *13*, 6. 10.3389/fnins.2019.00006.

1147 Hafemeister, C., and Satija, R. (2019). Normalization and variance stabilization of single-cell
1148 RNA-seq data using regularized negative binomial regression. Genome Biol *20*, 296.
1149 10.1186/s13059-019-1874-1.

1150 Haghverdi, L., Lun, A.T.L., Morgan, M.D., and Marioni, J.C. (2018). Batch effects in single-cell
1151 RNA-sequencing data are corrected by matching mutual nearest neighbors. Nat Biotechnol *36*,
1152 421-427. 10.1038/nbt.4091.

1153 Haring, M., Zeisel, A., Hochgerner, H., Rinwa, P., Jakobsson, J.E.T., Lonnerberg, P., La Manno,
1154 G., Sharma, N., Borgius, L., Kiehn, O., et al. (2018). Neuronal atlas of the dorsal horn defines its
1155 architecture and links sensory input to transcriptional cell types. Nat Neurosci *21*, 869-880.
1156 10.1038/s41593-018-0141-1.

1157 Hayashi, M., Hinckley, C.A., Driscoll, S.P., Moore, N.J., Levine, A.J., Hilde, K.L., Sharma, K., and
1158 Pfaff, S.L. (2018). Graded Arrays of Spinal and Supraspinal V2a Interneuron Subtypes Underlie
1159 Forelimb and Hindlimb Motor Control. Neuron *97*, 869-884 e865. 10.1016/j.neuron.2018.01.023.

1160 He, C.W., Liao, C.P., and Pan, C.L. (2018). Wnt signalling in the development of axon, dendrites
1161 and synapses. Open Biol *8*. 10.1098/rsob.180116.

1162 He, Z., and Jin, Y. (2016). Intrinsic Control of Axon Regeneration. Neuron *90*, 437-451.
1163 10.1016/j.neuron.2016.04.022.

1164 Hernandez-Miranda, L.R., Muller, T., and Birchmeier, C. (2017). The dorsal spinal cord and
1165 hindbrain: From developmental mechanisms to functional circuits. Dev Biol *432*, 34-42.
1166 10.1016/j.ydbio.2016.10.008.

1167 Hilton, B.J., Husch, A., Schaffran, B., Lin, T.C., Burnside, E.R., Dupraz, S., Schelski, M., Kim, J.,
1168 Muller, J.A., Schoch, S., et al. (2022). An active vesicle priming machinery suppresses axon
1169 regeneration upon adult CNS injury. Neuron *110*, 51-69 e57. 10.1016/j.neuron.2021.10.007.

1170 Horzmann, K.A., and Freeman, J.L. (2016). Zebrafish Get Connected: Investigating
1171 Neurotransmission Targets and Alterations in Chemical Toxicity. Toxics *4*.
1172 10.3390/toxics4030019.

1173 Hou, J., Bi, H., Ge, Q., Teng, H., Wan, G., Yu, B., Jiang, Q., and Gu, X. (2022). Heterogeneity
1174 analysis of astrocytes following spinal cord injury at single-cell resolution. FASEB J *36*, e22442.
1175 10.1096/fj.202200463R.

1176 Huang, C.X., Zhao, Y., Mao, J., Wang, Z., Xu, L., Cheng, J., Guan, N.N., and Song, J. (2021). An
1177 injury-induced serotonergic neuron subpopulation contributes to axon regrowth and function
1178 restoration after spinal cord injury in zebrafish. Nat Commun *12*, 7093. 10.1038/s41467-021-
1179 27419-w.

1180 Ilicic, T., Kim, J.K., Kolodziejczyk, A.A., Bagger, F.O., McCarthy, D.J., Marioni, J.C., and
1181 Teichmann, S.A. (2016). Classification of low quality cells from single-cell RNA-seq data. Genome
1182 Biol *17*, 29. 10.1186/s13059-016-0888-1.

1183 Isaacson, J.S., and Scanziani, M. (2011). How inhibition shapes cortical activity. Neuron *72*, 231-
1184 243. 10.1016/j.neuron.2011.09.027.

1185 Jankowski, M.P., McIlwrath, S.L., Jing, X., Cornuet, P.K., Salerno, K.M., Koerber, H.R., and
1186 Albers, K.M. (2009). Sox11 transcription factor modulates peripheral nerve regeneration in adult
1187 mice. Brain Res *1256*, 43-54. 10.1016/j.brainres.2008.12.032.

1188 Jin, S., Guerrero-Juarez, C.F., Zhang, L., Chang, I., Ramos, R., Kuan, C.H., Myung, P., Plikus,
1189 M.V., and Nie, Q. (2021). Inference and analysis of cell-cell communication using CellChat. Nat
1190 Commun *12*, 1088. 10.1038/s41467-021-21246-9.

1191 Jing, X., Wang, T., Huang, S., Glorioso, J.C., and Albers, K.M. (2012). The transcription factor
1192 Sox11 promotes nerve regeneration through activation of the regeneration-associated gene
1193 Sprr1a. Exp Neurol *233*, 221-232. 10.1016/j.expneurol.2011.10.005.

1194 Klatt Shaw, D., and Mokalled, M.H. (2021). Efficient CRISPR/Cas9 mutagenesis for
1195 neurobehavioral screening in adult zebrafish. G3 (Bethesda) *11*. 10.1093/g3journal/jkab089.

1196 Klatt Shaw, D., Saraswathy, V.M., Zhou, L., McAdow, A.R., Burris, B., Butka, E., Morris, S.A.,
1197 Dietmann, S., and Mokalled, M.H. (2021). Localized EMT reprograms glial progenitors to promote
1198 spinal cord repair. Dev Cell *56*, 613-626 e617. 10.1016/j.devcel.2021.01.017.

1199 Kole, C., Brommer, B., Nakaya, N., Sengupta, M., Bonet-Ponce, L., Zhao, T., Wang, C., Li, W.,
1200 He, Z., and Tomarev, S. (2020). Activating Transcription Factor 3 (ATF3) Protects Retinal
1201 Ganglion Cells and Promotes Functional Preservation After Optic Nerve Crush. Invest Ophthalmol
1202 Vis Sci *61*, 31. 10.1167/iovs.61.2.31.

1203 Kuscha, V., Frazer, S.L., Dias, T.B., Hibi, M., Becker, T., and Becker, C.G. (2012). Lesion-induced
1204 generation of interneuron cell types in specific dorsoventral domains in the spinal cord of adult
1205 zebrafish. J Comp Neurol *520*, 3604-3616. 10.1002/cne.23115.

1206 Lacar, B., Linker, S.B., Jaeger, B.N., Krishnaswami, S.R., Barron, J.J., Kelder, M.J.E., Parylak,
1207 S.L., Paquola, A.C.M., Venepally, P., Novotny, M., et al. (2016). Nuclear RNA-seq of single
1208 neurons reveals molecular signatures of activation. Nat Commun *7*, 11022.
1209 10.1038/ncomms11022.

1210 Lake, B.B., Codeluppi, S., Yung, Y.C., Gao, D., Chun, J., Kharchenko, P.V., Linnarsson, S., and
1211 Zhang, K. (2017). A comparative strategy for single-nucleus and single-cell transcriptomes
1212 confirms accuracy in predicted cell-type expression from nuclear RNA. Sci Rep *7*, 6031.
1213 10.1038/s41598-017-04426-w.

1214 Lange, M., Bergen, V., Klein, M., Setty, M., Reuter, B., Bakhti, M., Lickert, H., Ansari, M.,
1215 Schniering, J., Schiller, H.B., et al. (2022). CellRank for directed single-cell fate mapping. Nat
1216 Methods *19*, 159-170. 10.1038/s41592-021-01346-6.

1217 Lawson, N.D., Li, R., Shin, M., Grosse, A., Yukselen, O., Stone, O.A., Kucukural, A., and Zhu, L.
1218 (2020). An improved zebrafish transcriptome annotation for sensitive and comprehensive
1219 detection of cell type-specific genes. Elife *9*. 10.7554/eLife.55792.

1220 Levine, J.H., Simonds, E.F., Bendall, S.C., Davis, K.L., Amir el, A.D., Tadmor, M.D., Litvin, O.,
1221 Fienberg, H.G., Jager, A., Zunder, E.R., et al. (2015). Data-Driven Phenotypic Dissection of AML
1222 Reveals Progenitor-like Cells that Correlate with Prognosis. Cell *162*, 184-197.
1223 10.1016/j.cell.2015.05.047.

1224 Li, W.R., Wang, Y.L., Li, C., Gao, P., Zhang, F.F., Hu, M., Li, J.C., Zhang, S., Li, R., and Zhang,
1225 C.X. (2021). Synaptotagmin-11 inhibits spontaneous neurotransmission through vti1a. J
1226 Neurochem *159*, 729-741. 10.1111/jnc.15523.

1227 Lin, P.Y., Chanaday, N.L., Horvath, P.M., Ramirez, D.M.O., Monteggia, L.M., and Kavalali, E.T.
1228 (2020). VAMP4 Maintains a Ca(2+)-Sensitive Pool of Spontaneously Recycling Synaptic
1229 Vesicles. J Neurosci *40*, 5389-5401. 10.1523/JNEUROSCI.2386-19.2020.

1230 Lu, D.C., Niu, T., and Alaynick, W.A. (2015). Molecular and cellular development of spinal cord
1231 locomotor circuitry. Front Mol Neurosci *8*, 25. 10.3389/fnmol.2015.00025.

1232 Matson, K.J.E., Russ, D.E., Kathe, C., Hua, I., Maric, D., Ding, Y., Krynitsky, J., Pursley, R.,
1233 Sathyamurthy, A., Squair, J.W., et al. (2022). Single cell atlas of spinal cord injury in mice reveals
1234 a pro-regenerative signature in spinocerebellar neurons. Nat Commun *13*, 5628.
1235 10.1038/s41467-022-33184-1.

1236 Matson, K.J.E., Sathyamurthy, A., Johnson, K.R., Kelly, M.C., Kelley, M.W., and Levine, A.J.
1237 (2018). Isolation of Adult Spinal Cord Nuclei for Massively Parallel Single-nucleus RNA
1238 Sequencing. J Vis Exp. 10.3791/58413.

1239 McGinnis, C.S., Murrow, L.M., and Gartner, Z.J. (2019). DoubletFinder: Doublet Detection in
1240 Single-Cell RNA Sequencing Data Using Artificial Nearest Neighbors. Cell Syst *8*, 329-337 e324.
1241 10.1016/j.cels.2019.03.003.

1242 Milich, L.M., Choi, J.S., Ryan, C., Cerqueira, S.R., Benavides, S., Yahn, S.L., Tsoulfas, P., and
1243 Lee, J.K. (2021). Single-cell analysis of the cellular heterogeneity and interactions in the injured
1244 mouse spinal cord. J Exp Med *218*. 10.1084/jem.20210040.

1245 Milich, L.M., Ryan, C.B., and Lee, J.K. (2019). The origin, fate, and contribution of macrophages
1246 to spinal cord injury pathology. Acta Neuropathol *137*, 785-797. 10.1007/s00401-019-01992-3.

1247 Mokalled, M.H., Patra, C., Dickson, A.L., Endo, T., Stainier, D.Y., and Poss, K.D. (2016). Injury-
1248 induced ctgfa directs glial bridging and spinal cord regeneration in zebrafish. Science *354*, 630-
1249 634. 10.1126/science.aaf2679.

1250 Monaghan, J.R., Walker, J.A., Page, R.B., Putta, S., Beachy, C.K., and Voss, S.R. (2007). Early
1251 gene expression during natural spinal cord regeneration in the salamander Ambystoma
1252 mexicanum. J Neurochem *101*, 27-40. 10.1111/j.1471-4159.2006.04344.x.

1253 Nakamura, Y., Ueno, M., Niehaus, J.K., Lang, R.A., Zheng, Y., and Yoshida, Y. (2021).
1254 Modulation of Both Intrinsic and Extrinsic Factors Additively Promotes Rewiring of Corticospinal
1255 Circuits after Spinal Cord Injury. J Neurosci *41*, 10247-10260. 10.1523/JNEUROSCI.2649-
1256 20.2021.

1257 Nicholson-Fish, J.C., Kokotos, A.C., Gillingwater, T.H., Smillie, K.J., and Cousin, M.A. (2015).
1258 VAMP4 Is an Essential Cargo Molecule for Activity-Dependent Bulk Endocytosis. Neuron *88*, 973-
1259 984. 10.1016/j.neuron.2015.10.043.

1260 Park, K.K., Liu, K., Hu, Y., Smith, P.D., Wang, C., Cai, B., Xu, B., Connolly, L., Kramvis, I., Sahin,
1261 M., and He, Z. (2008). Promoting axon regeneration in the adult CNS by modulation of the
1262 PTEN/mTOR pathway. Science *322*, 963-966. 10.1126/science.1161566.

1263 R Core Team (2018). R: A language and environment for statistical computing. https://www.R-
1264 project.org/.

1265 Reimer, M.M., Kuscha, V., Wyatt, C., Sorensen, I., Frank, R.E., Knuwer, M., Becker, T., and
1266 Becker, C.G. (2009). Sonic hedgehog is a polarized signal for motor neuron regeneration in adult
1267 zebrafish. J Neurosci *29*, 15073-15082. 10.1523/JNEUROSCI.4748-09.2009.

1268 Reimer, M.M., Sorensen, I., Kuscha, V., Frank, R.E., Liu, C., Becker, C.G., and Becker, T. (2008).
1269 Motor neuron regeneration in adult zebrafish. The Journal of neuroscience : the official journal of
1270 the Society for Neuroscience *28*, 8510-8516. 10.1523/JNEUROSCI.1189-08.2008.

1271 Ren, Y., Ao, Y., O'Shea, T.M., Burda, J.E., Bernstein, A.M., Brumm, A.J., Muthusamy, N.,
1272 Ghashghaei, H.T., Carmichael, S.T., Cheng, L., and Sofroniew, M.V. (2017). Ependymal cell
1273 contribution to scar formation after spinal cord injury is minimal, local and dependent on direct
1274 ependymal injury. Sci Rep *7*, 41122. 10.1038/srep41122.

1275 Rodrigo Albors, A., Singer, G.A., Llorens-Bobadilla, E., Frisen, J., May, A.P., Ponting, C.P., and
1276 Storey, K.G. (2023). An ependymal cell census identifies heterogeneous and ongoing cell
1277 maturation in the adult mouse spinal cord that changes dynamically on injury. Dev Cell *58*, 239-
1278 255 e210. 10.1016/j.devcel.2023.01.003.

1279 Rosenberg, A.B., Roco, C.M., Muscat, R.A., Kuchina, A., Sample, P., Yao, Z., Graybuck, L.T.,
1280 Peeler, D.J., Mukherjee, S., Chen, W., et al. (2018). Single-cell profiling of the developing mouse
1281 brain and spinal cord with split-pool barcoding. Science *360*, 176-182. 10.1126/science.aam8999.

1282 Rossum, G.V., and Drake, F.L. (2009). Python 3 Reference Manual.

1283 Rougeot, J., Torraca, V., Zakrzewska, A., Kanwal, Z., Jansen, H.J., Sommer, F., Spaink, H.P.,
1284 and Meijer, A.H. (2019). RNAseq Profiling of Leukocyte Populations in Zebrafish Larvae Reveals
1285 a cxcl11 Chemokine Gene as a Marker of Macrophage Polarization During Mycobacterial
1286 Infection. Front Immunol *10*, 832. 10.3389/fimmu.2019.00832.

1287 Runker, A.E., Little, G.E., Suto, F., Fujisawa, H., and Mitchell, K.J. (2008). Semaphorin-6A
1288 controls guidance of corticospinal tract axons at multiple choice points. Neural Dev *3*, 34.
1289 10.1186/1749-8104-3-34.

1290 Salic, A., and Mitchison, T.J. (2008). A chemical method for fast and sensitive detection of DNA
1291 synthesis in vivo. Proc Natl Acad Sci U S A *105*, 2415-2420. 10.1073/pnas.0712168105.

1292 Saraswathy, V.M., Zhou, L., McAdow, A.R., Burris, B., Dogra, D., Reischauer, S., and Mokalled,
1293 M.H. (2022). Myostatin is a negative regulator of adult neurogenesis after spinal cord injury in
1294 zebrafish. Cell Rep *41*, 111705. 10.1016/j.celrep.2022.111705.

1295 Sathyamurthy, A., Johnson, K.R., Matson, K.J.E., Dobrott, C.I., Li, L., Ryba, A.R., Bergman, T.B.,
1296 Kelly, M.C., Kelley, M.W., and Levine, A.J. (2018). Massively Parallel Single Nucleus
1297 Transcriptional Profiling Defines Spinal Cord Neurons and Their Activity during Behavior. Cell
1298 Rep *22*, 2216-2225. 10.1016/j.celrep.2018.02.003.

1299 Satou, C., Kimura, Y., Hirata, H., Suster, M.L., Kawakami, K., and Higashijima, S. (2013).
1300 Transgenic tools to characterize neuronal properties of discrete populations of zebrafish neurons.
1301 Development *140*, 3927-3931. 10.1242/dev.099531.

1302 Scott, K., O'Rourke, R., Winkler, C.C., Kearns, C.A., and Appel, B. (2021). Temporal single-cell
1303 transcriptomes of zebrafish spinal cord pMN progenitors reveal distinct neuronal and glial
1304 progenitor populations. Dev Biol *479*, 37-50. 10.1016/j.ydbio.2021.07.010.

1305 Shah, P.T., Stratton, J.A., Stykel, M.G., Abbasi, S., Sharma, S., Mayr, K.A., Koblinger, K., Whelan,
1306 P.J., and Biernaskie, J. (2018). Single-Cell Transcriptomics and Fate Mapping of Ependymal Cells
1307 Reveals an Absence of Neural Stem Cell Function. Cell *173*, 1045-1057 e1049.
1308 10.1016/j.cell.2018.03.063.

1309 Shimada, T., Yoshida, T., and Yamagata, K. (2016). Neuritin Mediates Activity-Dependent Axonal
1310 Branch Formation in Part via FGF Signaling. J Neurosci *36*, 4534-4548.
1311 10.1523/JNEUROSCI.1715-15.2016.

1312 Shimojo, M., Madara, J., Pankow, S., Liu, X., Yates, J., 3rd, Sudhof, T.C., and Maximov, A. (2019).
1313 Synaptotagmin-11 mediates a vesicle trafficking pathway that is essential for development and
1314 synaptic plasticity. Genes Dev *33*, 365-376. 10.1101/gad.320077.118.

1315 Sofroniew, M.V. (2018). Dissecting spinal cord regeneration. Nature *557*, 343-350.
1316 10.1038/s41586-018-0068-4.

1317 Squair, J.W., Milano, M., de Coucy, A., Gautier, M., Skinnider, M.A., James, N.D., Cho, N., Lasne,
1318 A., Kathe, C., Hutson, T.H., et al. (2023). Recovery of walking after paralysis by regenerating
1319 characterized neurons to their natural target region. Science *381*, 1338-1345.
1320 10.1126/science.adi6412.

1321 Stassen, S.V., Yip, G.G.K., Wong, K.K.Y., Ho, J.W.K., and Tsia, K.K. (2021). Generalized and
1322 scalable trajectory inference in single-cell omics data with VIA. Nat Commun *12*, 5528.
1323 10.1038/s41467-021-25773-3.

1324 Sternberg, J.R., Prendergast, A.E., Brosse, L., Cantaut-Belarif, Y., Thouvenin, O., Orts-
1325 Del'Immagine, A., Castillo, L., Djenoune, L., Kurisu, S., McDearmid, J.R., et al. (2018). Pkd2l1 is
1326 required for mechanoception in cerebrospinal fluid-contacting neurons and maintenance of spine
1327 curvature. Nat Commun *9*, 3804. 10.1038/s41467-018-06225-x.

1328 Stuart, T., Butler, A., Hoffman, P., Hafemeister, C., Papalexi, E., Mauck, W.M., 3rd, Hao, Y.,
1329 Stoeckius, M., Smibert, P., and Satija, R. (2019). Comprehensive Integration of Single-Cell Data.
1330 Cell *177*, 1888-1902 e1821. 10.1016/j.cell.2019.05.031.

1331 Syed, D.S., Gowda, S.B., Reddy, O.V., Reichert, H., and VijayRaghavan, K. (2016). Glial and
1332 neuronal Semaphorin signaling instruct the development of a functional myotopic map for
1333 Drosophila walking. Elife *5*, e11572. 10.7554/eLife.11572.

1334 Tambalo, M., Mitter, R., and Wilkinson, D.G. (2020). A single cell transcriptome atlas of the
1335 developing zebrafish hindbrain. Development *147*. 10.1242/dev.184143.

1336 Tang, Q., Iyer, S., Lobbardi, R., Moore, J.C., Chen, H., Lareau, C., Hebert, C., Shaw, M.L., Neftel,
1337 C., Suva, M.L., et al. (2017). Dissecting hematopoietic and renal cell heterogeneity in adult
1338 zebrafish at single-cell resolution using RNA sequencing. J Exp Med *214*, 2875-2887.
1339 10.1084/jem.20170976.

1340 Tome, D., Dias, M.S., Correia, J., and Almeida, R.D. (2023). Fibroblast growth factor signaling in
1341 axons: from development to disease. Cell Commun Signal *21*, 290. 10.1186/s12964-023-01284-
1342 0.

1343 Tran, A.P., Warren, P.M., and Silver, J. (2022). New insights into glial scar formation after spinal
1344 cord injury. Cell Tissue Res *387*, 319-336. 10.1007/s00441-021-03477-w.

1345 Tsata, V., Mollmert, S., Schweitzer, C., Kolb, J., Mockel, C., Bohm, B., Rosso, G., Lange, C.,
1346 Lesche, M., Hammer, J., et al. (2021). A switch in pdgfrb(+) cell-derived ECM composition
1347 prevents inhibitory scarring and promotes axon regeneration in the zebrafish spinal cord. Dev Cell
1348 *56*, 509-524 e509. 10.1016/j.devcel.2020.12.009.

1349 van den Brink, S.C., Sage, F., Vertesy, A., Spanjaard, B., Peterson-Maduro, J., Baron, C.S.,
1350 Robin, C., and van Oudenaarden, A. (2017). Single-cell sequencing reveals dissociation-induced
1351 gene expression in tissue subpopulations. Nat Methods *14*, 935-936. 10.1038/nmeth.4437.

1352 Vandestadt, C., Vanwalleghem, G.C., Khabooshan, M.A., Douek, A.M., Castillo, H.A., Li, M.,
1353 Schulze, K., Don, E., Stamatis, S.A., Ratnadiwakara, M., et al. (2021). RNA-induced inflammation
1354 and migration of precursor neurons initiates neuronal circuit regeneration in zebrafish. Dev Cell
1355 *56*, 2364-2380 e2368. 10.1016/j.devcel.2021.07.021.

1356 Wang, C., Wang, Y., Hu, M., Chai, Z., Wu, Q., Huang, R., Han, W., Zhang, C.X., and Zhou, Z.
1357 (2016). Synaptotagmin-11 inhibits clathrin-mediated and bulk endocytosis. EMBO Rep *17*, 47-63.
1358 10.15252/embr.201540689.

1359 Wang, L.F., Huang, S.B., Zhao, H.D., Liu, C.J., Yao, L., and Shen, Y.Q. (2017). Activating
1360 transcription factor 3 promotes spinal cord regeneration of adult zebrafish. Biochem Biophys Res
1361 Commun *488*, 522-527. 10.1016/j.bbrc.2017.05.079.

1362 Wang, Z., Reynolds, A., Kirry, A., Nienhaus, C., and Blackmore, M.G. (2015). Overexpression of
1363 Sox11 promotes corticospinal tract regeneration after spinal injury while interfering with functional
1364 recovery. J Neurosci *35*, 3139-3145. 10.1523/JNEUROSCI.2832-14.2015.

1365 Wehner, D., Tsarouchas, T.M., Michael, A., Haase, C., Weidinger, G., Reimer, M.M., Becker, T.,
1366 and Becker, C.G. (2017). Wnt signaling controls pro-regenerative Collagen XII in functional spinal
1367 cord regeneration in zebrafish. Nat Commun *8*, 126. 10.1038/s41467-017-00143-0.

1368 Williams, R.R., Venkatesh, I., Pearse, D.D., Udvadia, A.J., and Bunge, M.B. (2015).
1369 MASH1/Ascl1a leads to GAP43 expression and axon regeneration in the adult CNS. PLoS One
1370 *10*, e0118918. 10.1371/journal.pone.0118918.

1371 Wu, H., Kirita, Y., Donnelly, E.L., and Humphreys, B.D. (2019). Advantages of Single-Nucleus
1372 over Single-Cell RNA Sequencing of Adult Kidney: Rare Cell Types and Novel Cell States
1373 Revealed in Fibrosis. J Am Soc Nephrol *30*, 23-32. 10.1681/ASN.2018090912.

1374 Xu, C., and Su, Z. (2015). Identification of cell types from single-cell transcriptomes using a novel
1375 clustering method. Bioinformatics *31*, 1974-1980. 10.1093/bioinformatics/btv088.

1376 Yadav, A., Matson, K.J.E., Li, L., Hua, I., Petrescu, J., Kang, K., Alkaslasi, M.R., Lee, D.I., Hasan,
1377 S., Galuta, A., et al. (2023). A cellular taxonomy of the adult human spinal cord. Neuron *111*, 328-
1378 344 e327. 10.1016/j.neuron.2023.01.007.

1379 Yang, S., Corbett, S.E., Koga, Y., Wang, Z., Johnson, W.E., Yajima, M., and Campbell, J.D.
1380 (2020). Decontamination of ambient RNA in single-cell RNA-seq with DecontX. Genome Biol *21*,
1381 57. 10.1186/s13059-020-1950-6.

1382 Yao, C., Cao, Y., Wang, D., Lv, Y., Liu, Y., Gu, X., Wang, Y., Wang, X., and Yu, B. (2022). Single-
1383 cell sequencing reveals microglia induced angiogenesis by specific subsets of endothelial cells
1384 following spinal cord injury. FASEB J *36*, e22393. 10.1096/fj.202200337R.

1385 Ye, L.X., An, N.C., Huang, P., Li, D.H., Zheng, Z.L., Ji, H., Li, H., Chen, D.Q., Wu, Y.Q., Xiao, J.,
1386 et al. (2021). Exogenous platelet-derived growth factor improves neurovascular unit recovery after
1387 spinal cord injury. Neural Regen Res *16*, 765-771. 10.4103/1673-5374.295347.

1388 Yoshida, Y. (2012). Semaphorin signaling in vertebrate neural circuit assembly. Front Mol
1389 Neurosci *5*, 71. 10.3389/fnmol.2012.00071.

1390 Zappia, L., and Oshlack, A. (2018). Clustering trees: a visualization for evaluating clusterings at
1391 multiple resolutions. Gigascience *7*. 10.1093/gigascience/giy083.

1392 Zavvarian, M.M., Zhou, C., Kahnemuyipour, S., Hong, J., and Fehlings, M.G. (2021). The MAPK
1393 Signaling Pathway Presents Novel Molecular Targets for Therapeutic Intervention after Traumatic
1394 Spinal Cord Injury: A Comparative Cross-Species Transcriptional Analysis. Int J Mol Sci *22*.
1395 10.3390/ijms222312934.

1396 Zeisel, A., Hochgerner, H., Lonnerberg, P., Johnsson, A., Memic, F., van der Zwan, J., Haring,
1397 M., Braun, E., Borm, L.E., La Manno, G., et al. (2018). Molecular Architecture of the Mouse
1398 Nervous System. Cell *174*, 999-1014 e1022. 10.1016/j.cell.2018.06.021.

1399 Zhang, H., Fang, X., Huang, D., Luo, Q., Zheng, M., Wang, K., Cao, L., and Yin, Z. (2018).
1400 Erythropoietin signaling increases neurogenesis and oligodendrogenesis of endogenous neural
1401 stem cells following spinal cord injury both in vivo and in vitro. Mol Med Rep *17*, 264-272.
1402 10.3892/mmr.2017.7873.

1403 Zhang, Y., Bo, X., Schoepfer, R., Holtmaat, A.J., Verhaagen, J., Emson, P.C., Lieberman, A.R.,
1404 and Anderson, P.N. (2005). Growth-associated protein GAP-43 and L1 act synergistically to
1405 promote regenerative growth of Purkinje cell axons in vivo. Proc Natl Acad Sci U S A *102*, 14883-
1406 14888. 10.1073/pnas.0505164102.

1407 Zhang, Y., Chen, K., Sloan, S.A., Bennett, M.L., Scholze, A.R., O'Keeffe, S., Phatnani, H.P.,
1408 Guarnieri, P., Caneda, C., Ruderisch, N., et al. (2014). An RNA-sequencing transcriptome and
1409 splicing database of glia, neurons, and vascular cells of the cerebral cortex. J Neurosci *34*, 11929-
1410 11947. 10.1523/JNEUROSCI.1860-14.2014.

1411 Zhang, Y., Sloan, S.A., Clarke, L.E., Caneda, C., Plaza, C.A., Blumenthal, P.D., Vogel, H.,
1412 Steinberg, G.K., Edwards, M.S., Li, G., et al. (2016). Purification and Characterization of
1413 Progenitor and Mature Human Astrocytes Reveals Transcriptional and Functional Differences
1414 with Mouse. Neuron *89*, 37-53. 10.1016/j.neuron.2015.11.013.

1415 Zhou, Y., Zhou, B., Pache, L., Chang, M., Khodabakhshi, A.H., Tanaseichuk, O., Benner, C., and
1416 Chanda, S.K. (2019). Metascape provides a biologist-oriented resource for the analysis of
1417 systems-level datasets. Nat Commun *10*, 1523. 10.1038/s41467-019-09234-6.

1418

Figure 1

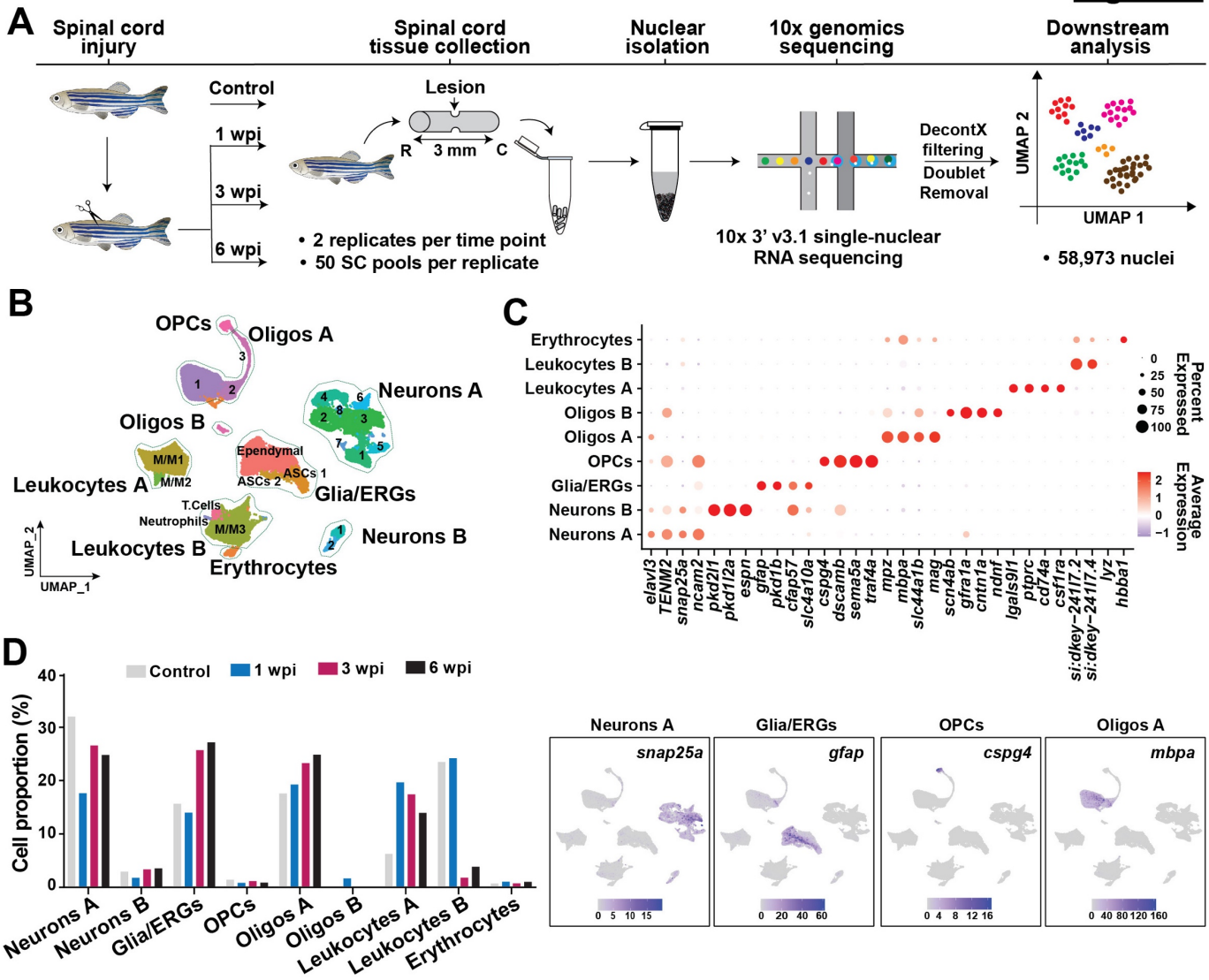
A
Spinal cord injury
Spinal cord tissue collection
Nuclear isolation
10x genomics sequencing
Downstream analysis
Control
1 wpi
3 wpi
6 wpi
Lesion
R
3 mm
C
• 2 replicates per time point
• 50 SC pools per replicate
DecontX filtering
Doublet Removal
10x 3' v3.1 single-nuclear RNA sequencing
UMAP 2
UMAP 1
• 58,973 nuclei
B
OPCs
Oligos A
Oligos B
Neurons A
Ependymal
ASCs 1
ASCs 2
Glia/ERGs
M/M1
M/M2
Leukocytes A
T.Cells
Neutrophils
M/M3
Leukocytes B
Erythrocytes
Neurons B
UMAP_2
UMAP_1
C
Erythrocytes
Leukocytes B
Leukocytes A
Oligos B
Oligos A
OPCs
Glia/ERGs
Neurons B
Neurons A
elavl3
TENM2
snap25a
ncam2
pkd2l1
pkd1l2a
espn
gfap
pkd1b
cfap57
slc4a10a
cspg4
dscamb
sema5a
traf4a
mpz
mbpa
slc44a1b
mag
scn4ab
gfra1a
cntn1a
ndnf
lgals9l1
ptprc
cd74a
csf1ra
si:dkey-241l7.2
si:dkey-241l7.4
lyz
hbba1
Percent Expressed
Average Expression
D
Control
1 wpi
3 wpi
6 wpi
Cell proportion (%)
Neurons A
Neurons B
Glia/ERGs
OPCs
Oligos A
Oligos B
Leukocytes A
Leukocytes B
Erythrocytes
snap25a
gfap
cspg4
mbpa
E
Neurons B
OPCs
Oligos B
Erythrocytes
Neurons A
Glia/ERGs
Oligos A
Leukocytes A
Leukocytes B
Expression

888 **Figure 1. Transcriptomic profiling of innate SC repair in adult zebrafish. (A)** Experimental
889 pipeline to generate a single-cell atlas of zebrafish cells after SCI. SC tissue collection, nuclear
890 isolation and single nuclear RNA-seq (snRNA-seq) were performed on wild-type fish at 1, 3 and
891 6 wpi. Uninjured SC nuclei were used as 0 wpi controls. 10x genomics sequencing with v3.1
892 chemistry was performed. Two biological replicates were used at each time point, and SC tissues
893 from 50 animals were pooled into a single biological replicate. **(B)** Merged UMAP representation
894 of the complete dataset. Two biological replicates, 4 time points and 58,973 cells were clustered
895 into major spinal cell populations including Neurons A and B, glia/ependymo-radial glial cells
896 (glia/ERGs), oligodendrocyte precursor cells (OPCs), oligodendrocytes A and B, Leukocytes A
897 and B, and Erythrocytes. **(C)** Marker gene expression in the major cell types identified after SCI.
898 Dot plot shows canonical marker genes are enriched in their respective cell types identified. Dot
899 colors and diameters represent average gene expression and percent cells with at least one UMI
900 detected per gene, respectively. Feature plots depicting the distributions of canonical marker
901 genes corresponding to the major cell populations are shown. **(D)** Distribution of major cell types
902 during SC regeneration. For each time point, cell proportions were normalized to the total number
903 of cells present at that time point. **(E)** Heatmap showing top 10 differentially expressed (DE)
904 genes in the major cell populations identified by snRNA-seq. Yellow and magenta represent highly
905 enriched and low-expression genes, respectively.

Figure 2

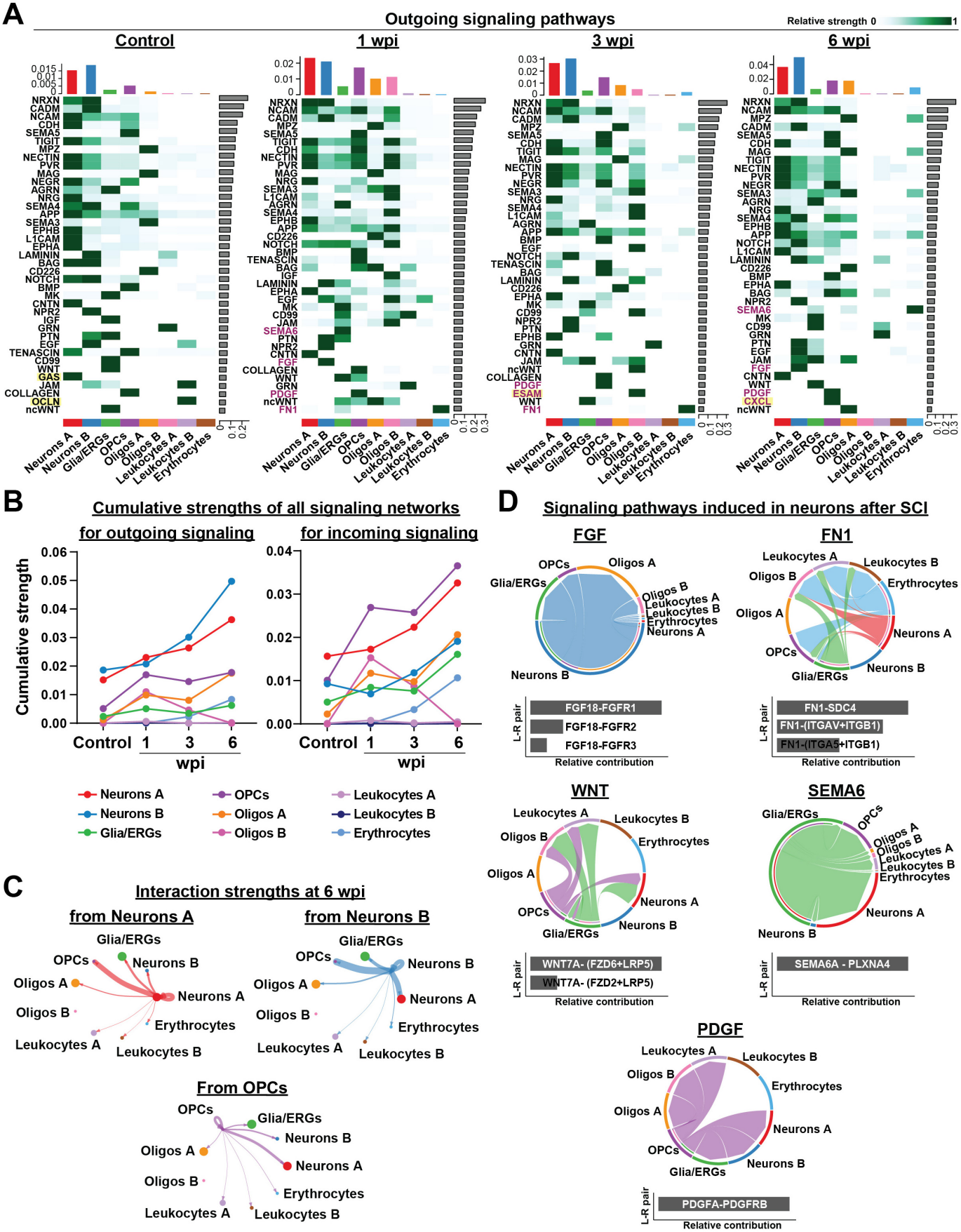
A
Outgoing signaling pathways
Relative strength 0 1
Control
1 wpi
3 wpi
6 wpi
Neurons A
Neurons B
Glia/ERGs
OPCs
Oligos A
Oligos B
Leukocytes A
Leukocytes B
Erythrocytes
B
Cumulative strengths of all signaling networks
for outgoing signaling
for incoming signaling
Cumulative strength
Control 1 3 6
wpi
Neurons A
Neurons B
Glia/ERGs
OPCs
Oligos A
Oligos B
Leukocytes A
Leukocytes B
Erythrocytes
C
Interaction strengths at 6 wpi
from Neurons A
from Neurons B
From OPCs
D
Signaling pathways induced in neurons after SCI
FGF
FN1
WNT
SEMA6
PDGF
L-R pair
FGF18-FGFR1
FGF18-FGFR2
FGF18-FGFR3
FN1-SDC4
FN1-(ITGAV+ITGB1)
FN1-(ITGA5+ITGB1)
WNT7A- (FZD6+LRP5)
WNT7A- (FZD2+LRP5)
SEMA6A - PLXNA4
PDGFA-PDGFRB
Relative contribution

906 **Figure 2. Cell-cell interaction networks during SC regeneration. (A)** Relative strengths of
907 outgoing signaling pathways in major spinal cell populations at 0, 1, 3 and 6 wpi. Bar graphs at
908 the top of each heatmap show cumulative signaling strengths per cell population. Bar graphs at
909 the right of each heatmap show cumulative signaling strength per pathway. Pathways highlighted
910 in yellow are specifically enriched at one time point. Pathways highlighted in magenta are
911 enriched after injury. **(B)** Cumulative strengths of signaling pathways outgoing from or received
912 by major cell types. **(C)** Circle plots represent cell-cell interaction strengths of signaling pathways
913 outgoing from Neurons A, B and OPCs at 6 wpi. Arrow thickness is directly proportional to the
914 cumulative strengths of all predicted interactions between clusters. **(D)** Chord diagrams showing
915 intercellular communication of signaling pathways that are enriched in neurons after SCI. Arc
916 diameters are proportional to cumulative signaling strengths. Bar graphs at the bottom of each
917 chord diagram represent the relative contribution of different ligand-receptor pairs predicted for
918 the corresponding signaling pathway.

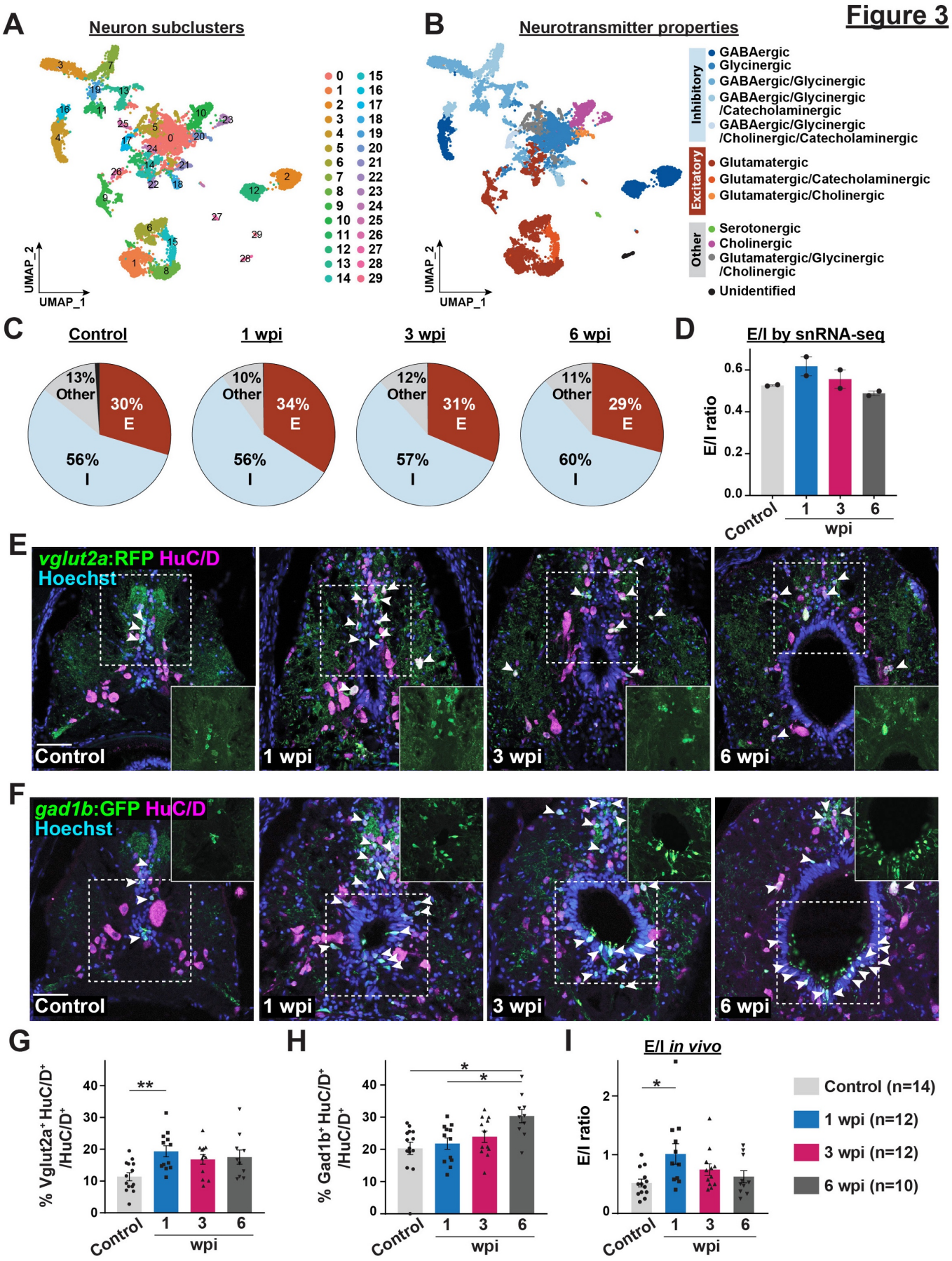
Figure 3
A
Neuron subclusters
UMAP_2
UMAP_1
0 1 2 3 4 5 6 7 8 9 10 11 12 13 14 15 16 17 18 19 20 21 22 23 24 25 26 27 28 29
B
Neurotransmitter properties
Inhibitory
GABAergic
Glycinergic
GABAergic/Glycinergic
GABAergic/Glycinergic /Catecholaminergic
GABAergic/Glycinergic /Cholinergic/Catecholaminergic
Excitatory
Glutamatergic
Glutamatergic/Catecholaminergic
Glutamatergic/Cholinergic
Other
Serotonergic
Cholinergic
Glutamatergic/Glycinergic /Cholinergic
Unidentified
C
Control
1 wpi
3 wpi
6 wpi
13% Other
30% E
56% I
10% Other
34% E
56% I
12% Other
31% E
57% I
11% Other
29% E
60% I
D
E/I by snRNA-seq
E/I ratio
0.0
0.2
0.4
0.6
Control
1
3
6
wpi
E
vglut2a:RFP HuC/D
Hoechst
Control
1 wpi
3 wpi
6 wpi
F
gad1b:GFP HuC/D
Hoechst
Control
1 wpi
3 wpi
6 wpi
G
% Vglut2a+ HuC/D+ /HuC/D+
0
10
20
30
40
**
Control
1
3
6
wpi
H
% Gad1b+ HuC/D+ /HuC/D+
0
10
20
30
40
*
*
Control
1
3
6
wpi
I
E/I in vivo
E/I ratio
0
1
2
*
Control
1
3
6
wpi
Control (n=14)
1 wpi (n=12)
3 wpi (n=12)
6 wpi (n=10)

919 **Figure 3. Recovery of excitatory/inhibitory balance during SC regeneration. (A)** UMAP plot
920 showing 30 different neuron subclusters identified with 0.6 resolution parameter. **(B)** Classification
921 of neuron clusters based on neurotransmitter properties. Canonical neurotransmitter marker
922 genes are used: *slc17a6a* and *slc17a6b* for glutamatergic neurons; *slc6a5, gad1a, gad1b* and
923 *gad2* for GABA/glycinergic neurons; *chata and slc5a7a* for cholinergic neurons; *slc6a4a* and *tph2*
924 for serotonergic neurons and *slc6a2* for catecholaminergic neurons. Clusters with enrichment of
925 at least one of the glutamatergic markers are identified as excitatory and with enrichment of at
926 least one of the GABA/glycinergic markers are identified as inhibitory. Clusters that only show
927 enrichment for serotonergic, cholinergic, or a mix of glutamatergic and glycinergic markers are
928 labelled as "Other". The neuron cluster that does not express any of the previously mentioned
929 marker genes is labelled "Unidentified". **(C)** Pie charts show the proportions of excitatory,
930 inhibitory, and "Other" neuron populations at 0, 1, 3 and 6 wpi. **(D)** *in silico* calculation of E/I ratios
931 during SC regeneration. Bar charts depict the ratio between excitatory and inhibitory neurons at
932 0, 1, 3 and 6 wpi. Dots indicate single biological replicates. Two biological replicates are shown
933 per time point. Error bars represent SEM. **(E, F)** Immunostaining for RFP, GFP, HuC/D and
934 Hoechst in SC cross sections from Tg(*vglut2a*:RFP) and Tg(*gad1b*:GFP) zebrafish at 0, 1, 3 and
935 6 wpi. White arrows point to RFP^+ HuC/D^+ neurons in E and GFP^+ HuC/D^+ neurons in F. Insets
936 depict single channel views of *vglut2a*:RFP or *gad1b*:GFP in dorsal and ventral SC domains,
937 respectively. **(G, H)** Quantification of glutamatergic and GABAergic neurons after SCI. Percent
938 *vglut2a*$^+$ HuC/D^+ neurons (ANOVA p-value: 0.0086) and *gad1b*$^+$ HuC/D^+ neurons (ANOVA p-
939 value: 0.0043) were normalized to the total number of HuC/D^+ neurons. **(I)** *in vivo* quantification
940 of E/I ratios during SC regeneration. Ratios of glutamatergic to GABAergic neurons were
941 calculated at 0, 1, 3 and 6 wpi (ANOVA p-value: 0.03421). Solid circles and polygons in bar charts
942 indicate individual animals and sample sizes are indicated in parentheses. SC cross sections 450
943 µm rostral to the lesion were analyzed. Brown-Forsythe and Welch ANOVA test was performed
944 in G, H and I with Dunnett's T3 multiple comparisons test performed across different time points
945 having 95% CI. * $p \leq 0.05$, ** $p \leq 0.01$; Scale bars, 50 µm.

Figure 4

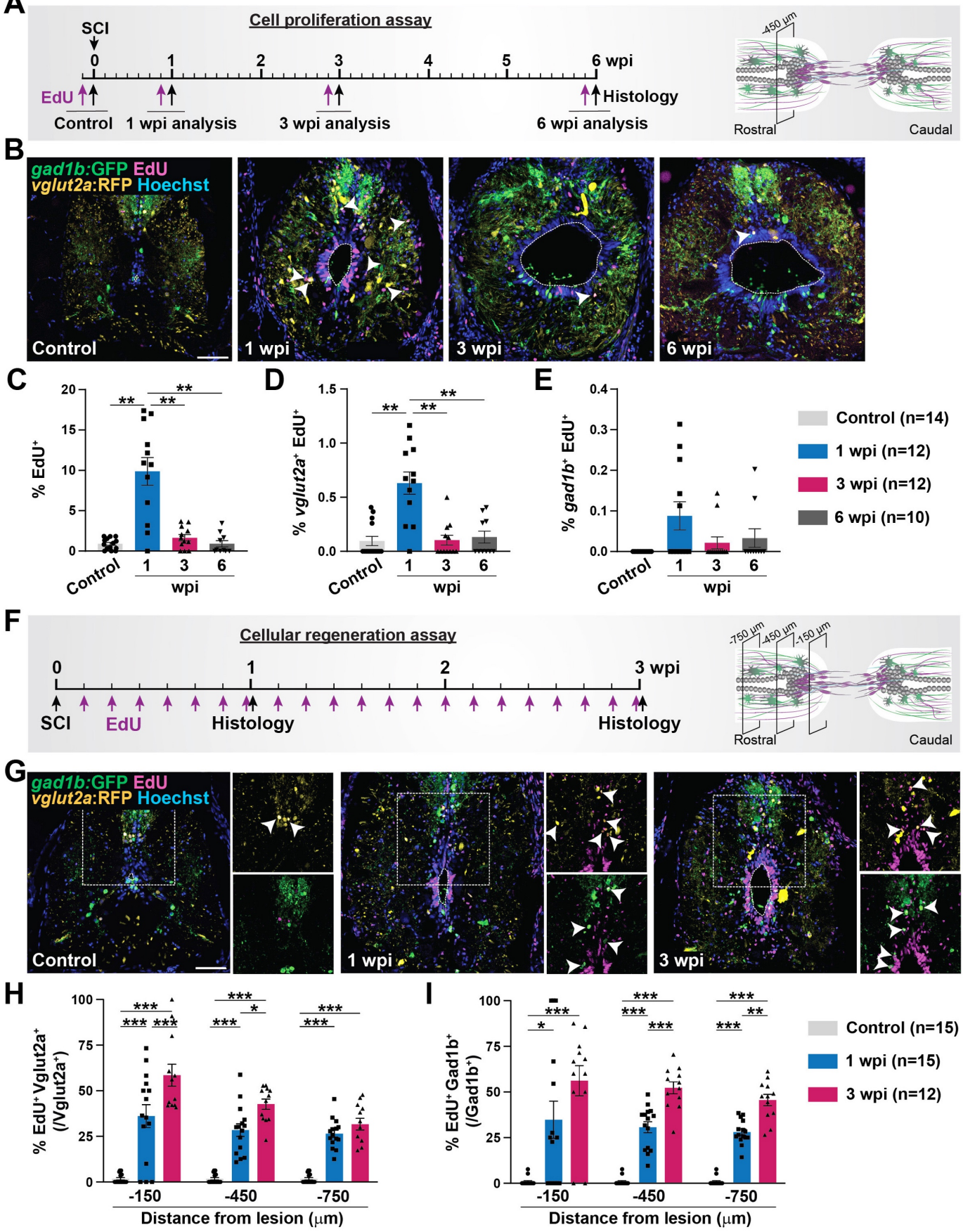
A
Cell proliferation assay
SCI
0
1
2
3
4
5
6 wpi
EdU
Histology
Control
1 wpi analysis
3 wpi analysis
6 wpi analysis
-450 µm
Rostral
Caudal
B
gad1b:GFP EdU
vglut2a:RFP Hoechst
Control
1 wpi
3 wpi
6 wpi
C
% EdU+
Control
1
3
6
wpi
D
% vglut2a+ EdU+
E
% gad1b+ EdU+
Control (n=14)
1 wpi (n=12)
3 wpi (n=12)
6 wpi (n=10)
F
Cellular regeneration assay
0
1
2
3 wpi
SCI
EdU
Histology
Histology
-750 µm
-450 µm
-150 µm
Rostral
Caudal
G
gad1b:GFP EdU
vglut2a:RFP Hoechst
Control
1 wpi
3 wpi
H
% EdU+Vglut2a+ (/Vglut2a+)
-150
-450
-750
Distance from lesion (µm)
I
% EdU+Gad1b+ (/Gad1b+)
Control (n=15)
1 wpi (n=15)
3 wpi (n=12)

946 **Figure 4. Regeneration of excitatory and inhibitory neurons after SCI. (A)** Experimental
947 timeline to assess cell proliferation at 1, 3 and 6 wpi. Tg(*vglut2a*:RFP; *gad1b*:GFP) zebrafish were
948 subjected to SC transections. Single intraperitoneal EdU injections were performed at either 6,
949 20, or 41 days post-injury. SC tissues were harvested for analysis at 1, 3, or 6 wpi and at 24 hours
950 after EdU injection. Uninjured animals were injected with EdU and collected 24 hours after EdU
951 injection as controls. SC cross-section 450 µm rostral to the lesion was used for quantifications.
952 **(B)** Staining for RFP, GFP, EdU and Hoechst in SC cross sections of Tg(*vglut2a*:RFP;
953 *gad1b*:GFP) zebrafish at 0, 1, 3 and 6 wpi. White arrows indicate *vglut2a*$^+$ EdU$^+$ neurons. Dotted
954 lines delineate central canal edges. **(C-E)** Quantification of EdU$^+$ cells (ANOVA p-value <0.0001),
955 *vglut2a*$^+$ EdU$^+$ neurons (ANOVA p-value <0.0001) and *gad1b*$^+$ EdU$^+$ neurons (ANOVA p-value:
956 0.0449) at 0, 1, 3 and 6 wpi. Percent cells were normalized to the total number of nuclei in SC
957 sections. **(F)** Experimental timeline to assess the cumulative profiles of regenerating neurons at
958 1 and 3 wpi. Tg(*vglut2a*:RFP; *gad1b*:GFP) zebrafish were subjected to SC transections and daily
959 intraperitoneal EdU injections. SC tissues were harvested for analysis at 1 and 3 wpi. Control SCs
960 received daily EdU injection for 7 days before collection. Tissue sections 150, 450 and 750 µm
961 rostral to the lesion were analyzed. **(G)** Staining for RFP, GFP, EdU and Hoechst in SC cross
962 sections of Tg(*vglut2a*:RFP; *gad1b*:GFP) zebrafish at 0, 1 and 3 wpi. White arrows indicate
963 *vglut2a*$^+$ EdU$^+$ neurons. Insets show single channel views of *vglut2a*:RFP and *gad1b*:GFP
964 expression. Dotted lines delineate central canal edges. **(H, I)** Quantification of regenerating
965 glutamatergic neurons (*vglut2a*$^+$ EdU$^+$) (ANOVA p-value <0.0001) and regenerating GABAergic
966 neurons (*gad1b*$^+$ EdU$^+$) (ANOVA p-value <0.0001). For each section, percent cells were
967 normalized to the number of *vglut2a*$^+$ EdU$^+$ neurons in H and *vglut2a*$^+$ EdU$^+$ neurons in I. Brown-
968 Forsythe and Welch ANOVA test were performed in C, D and E with Dunnett's T3 multiple
969 comparisons test performed across different time points with 95% CI. Two-way ANOVA was
970 performed in H and I with Tukey's multiple comparison test having 95% CI. * p≤0.05, ** p ≤0.01,
971 *** p≤0.001. Solid circles and polygons in the bar charts indicate individual animals and sample
972 sizes are indicated in parentheses. Scale bars, 50 µm.

Figure 5

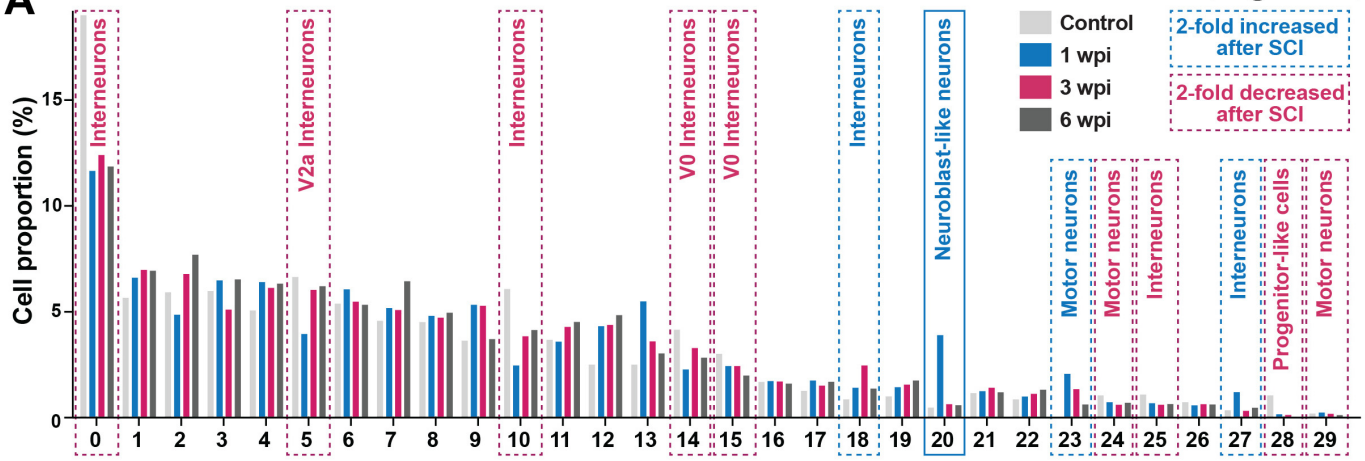
A
Cell proportion (%)
Control
1 wpi
3 wpi
6 wpi
2-fold increased after SCI
2-fold decreased after SCI
Interneurons
V2a Interneurons
V0 Interneurons
Neuroblast-like neurons
Motor neurons
Progenitor-like cells

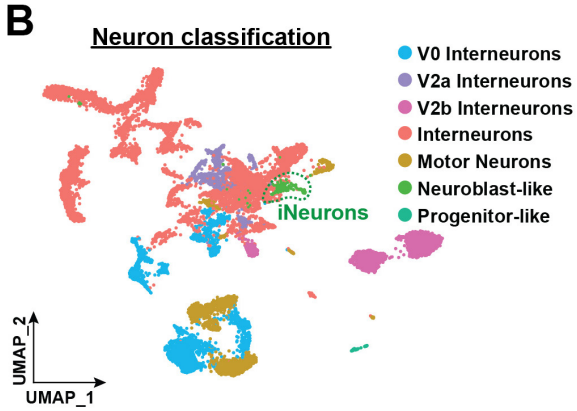
B
Neuron classification
V0 Interneurons
V2a Interneurons
V2b Interneurons
Interneurons
Motor Neurons
Neuroblast-like
Progenitor-like
iNeurons
UMAP_2
UMAP_1

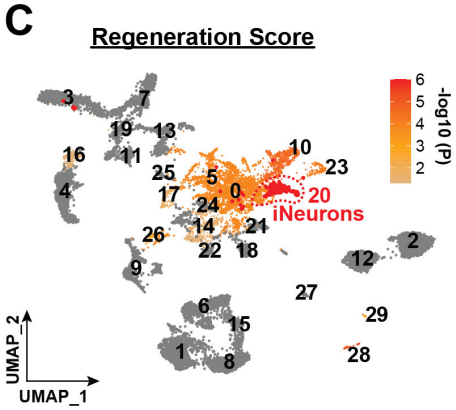
C
Regeneration Score
-log10 (P)
iNeurons
UMAP_2
UMAP_1

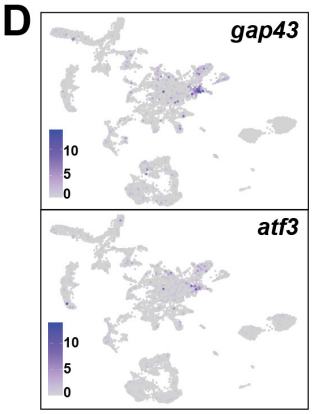
D
gap43
atf3

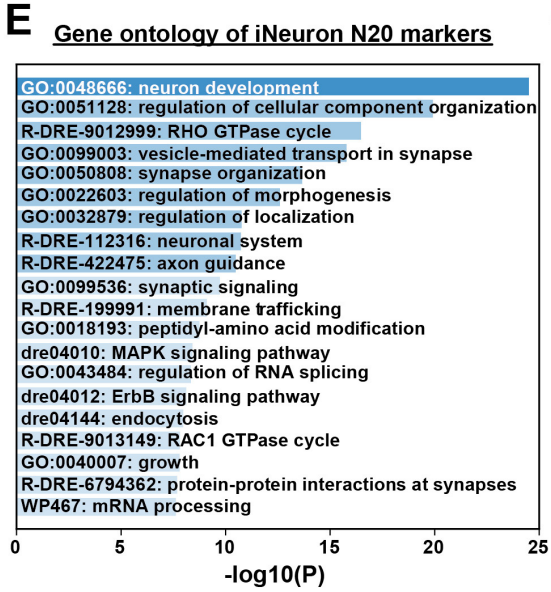
E
Gene ontology of iNeuron N20 markers
GO:0048666: neuron development
GO:0051128: regulation of cellular component organization
R-DRE-9012999: RHO GTPase cycle
GO:0099003: vesicle-mediated transport in synapse
GO:0050808: synapse organization
GO:0022603: regulation of morphogenesis
GO:0032879: regulation of localization
R-DRE-112316: neuronal system
R-DRE-422475: axon guidance
GO:0099536: synaptic signaling
R-DRE-199991: membrane trafficking
GO:0018193: peptidyl-amino acid modification
dre04010: MAPK signaling pathway
GO:0043484: regulation of RNA splicing
dre04012: ErbB signaling pathway
dre04144: endocytosis
R-DRE-9013149: RAC1 GTPase cycle
GO:0040007: growth
R-DRE-6794362: protein-protein interactions at synapses
WP467: mRNA processing
-log10(P)

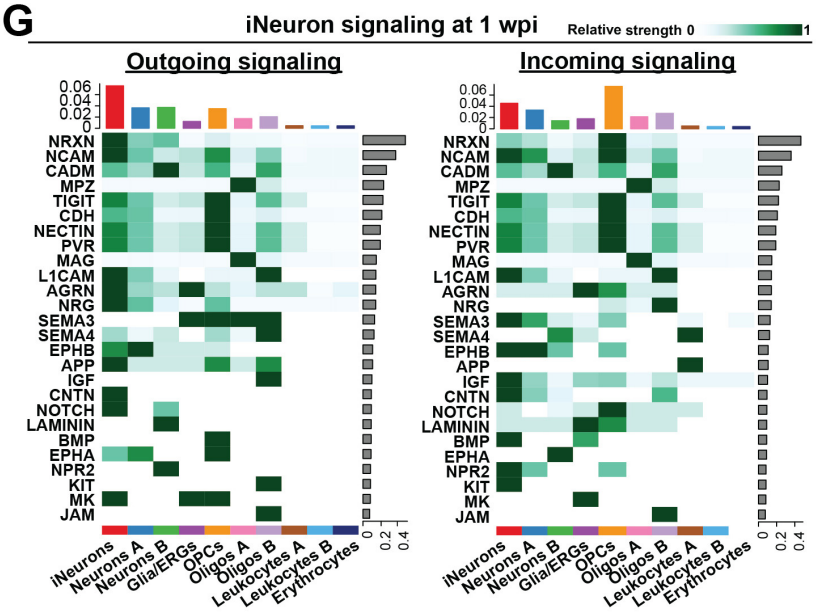
G
iNeuron signaling at 1 wpi
Relative strength
Outgoing signaling
Incoming signaling
NRXN
NCAM
CADM
MPZ
TIGIT
CDH
NECTIN
PVR
MAG
L1CAM
AGRN
NRG
SEMA3
SEMA4
EPHB
APP
IGF
CNTN
NOTCH
LAMININ
BMP
EPHA
NPR2
KIT
MK
JAM
iNeurons
Neurons A
Neurons B
Glia/ERGs
OPCs
Oligos A
Oligos B
Leukocytes A
Leukocytes B
Erythrocytes

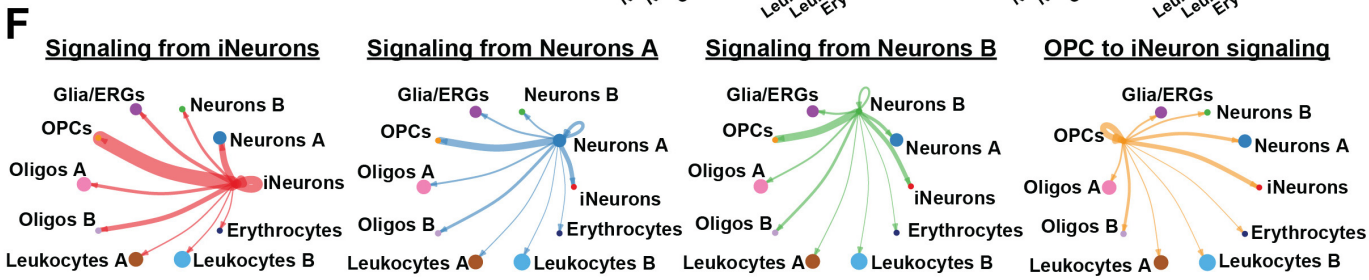
F
Signaling from iNeurons
Signaling from Neurons A
Signaling from Neurons B
OPC to iNeuron signaling
Glia/ERGs
Neurons B
OPCs
Neurons A
Oligos A
iNeurons
Oligos B
Erythrocytes
Leukocytes A
Leukocytes B

973 **Figure 5. Emergence of an injury-responsive iNeuron signature during SC regeneration.**
974 **(A)** Dynamics of neuronal subclusters at 0, 1, 3 and 6 wpi. Cell proportions for each cluster and
975 time point were normalized to the total number of neurons analyzed at that time point. Clusters
976 that either increased or decreased by >2-fold in proportion are highlighted in red and blue,
977 respectively. **(B)** UMAP plot showing predicted cluster identity for each neuron subpopulations.
978 V0, V2a, V2b, interneurons, motor neurons are shown along with clusters identified as neuroblast-
979 like or progenitor-like neurons. Cluster N20 was the only cluster identified as neuroblast-like
980 neurons. **(C)** UMAP plot showing Regeneration score for each neuron subclusters. -log10P value
981 of each cluster is represented in a gradient scale of gray (min=0) to red (max=6). Cluster N20
982 showed the highest regeneration score compared to all other neurons. **(D)** Feature plots show
983 the expression of the regeneration associated genes *gap43* and *atf3* in cluster N20. **(E)** Gene
984 ontology of N20 iNeuron DE markers. Twenty of the most enriched terms are shown. X-axis
985 represents -log10(p-value) for each term. **(F)** Circle plots represent cell-cell interaction strengths
986 at 1 wpi. Arrow thickness is directly proportional to the cumulative strengths of all predicted
987 interactions between clusters. **(G)** Signaling pathways outgoing from or received by iNeurons at
988 1 wpi. Bar graphs at the top of each heatmap show cumulative signaling strengths per cell
989 population. Bar graphs at the right of each heatmap show cumulative signaling strength per
990 pathway.

Figure 6

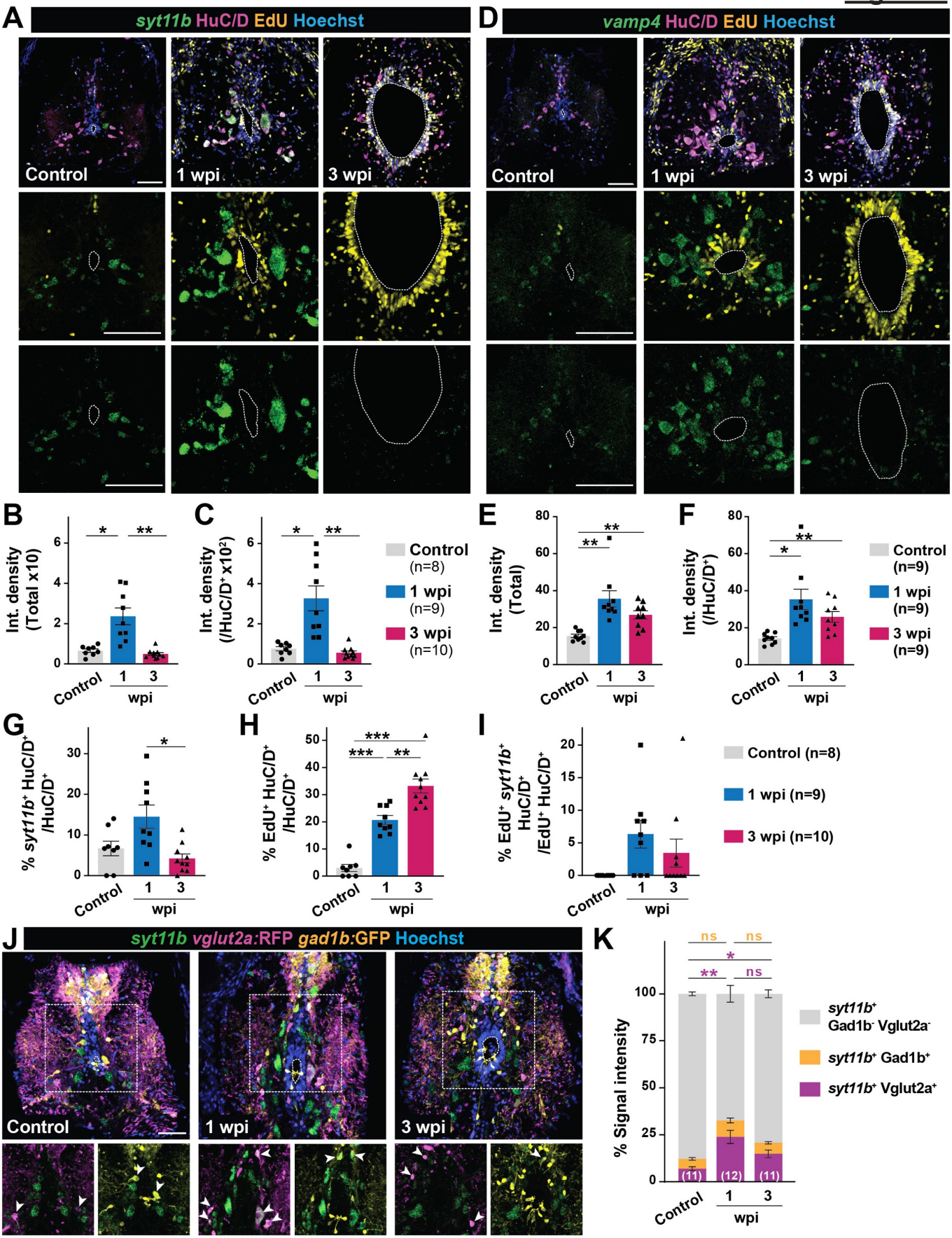
A
syt11b HuC/D EdU Hoechst
Control
1 wpi
3 wpi
D
vamp4 HuC/D EdU Hoechst
Control
1 wpi
3 wpi
B
Int. density (Total x10)
Control
1
3
wpi
C
Int. density (/HuC/D+ x10²)
Control (n=8)
1 wpi (n=9)
3 wpi (n=10)
E
Int. density (Total)
F
Int. density (/HuC/D+)
Control (n=9)
1 wpi (n=9)
3 wpi (n=9)
G
% syt11b+ HuC/D+ /HuC/D+
H
% EdU+ HuC/D+ /HuC/D+
I
% EdU+ syt11b+ HuC/D+ /EdU+ HuC/D+
Control (n=8)
1 wpi (n=9)
3 wpi (n=10)
J
syt11b vglut2a:RFP gad1b:GFP Hoechst
Control
1 wpi
3 wpi
K
% Signal intensity
ns
*
**
syt11b+ Gad1b- Vglut2a-
syt11b+ Gad1b+
syt11b+ Vglut2a+
(11)
(12)
(11)
Control
1
3
wpi

991 **Figure 6. *in vivo* mapping of iNeurons in zebrafish spinal tissues. (A)** HCR *in situ*
992 hybridization for *syt11b* and staining for HuC/D, Hoechst and EdU were performed on wild-type
993 SC cross sections at 0, 1 and 3 wpi. Dotted lines delineate central canal edges. **(B, C)**
994 Quantification of *syt11b* HCR *in situ* hybridization. Integrated density was calculated in the whole
995 SC cross sections (ANOVA p-value: 0.0007) and inside HuC/D$^+$ neurons (ANOVA p-value:
996 0.0009) at 0, 1 and 3 wpi. **(D)** HCR *in situ* hybridization for *vamp4* and staining for HuC/D, Hoechst
997 and EdU were performed on wild-type SC cross sections at 0, 1 and 3 wpi. Dotted lines delineate
998 central canal edges. **(E, F)** Quantification of *vamp4* HCR *in situ* hybridization. Integrated density
999 was calculated in the whole SC cross sections (ANOVA p-value: 0.0012) and inside HuC/D$^+$
1000 neurons (ANOVA p-value: 0.0043) at 0, 1 and 3 wpi. **(G-I)** Quantification of *syt11b* expressing
1001 cells after SCI. Percent *syt11b*$^+$ HuC/D$^+$ neurons (normalized to HuC/D$^+$ neurons in G) (ANOVA p-
1002 value: 0.0062), percent EdU$^+$ HuC/D$^+$ neurons (normalized to HuC/D$^+$ neurons in H) (ANOVA p-
1003 value <0.0001), and percent *syt11b*$^+$ EdU$^+$ HuC/D$^+$ neurons (normalized to EdU$^+$ HuC/D$^+$ neurons
1004 in I) (ANOVA p-value: 0.0813). Analysis was performed on SC cross sections at 0, 1 and 3 wpi.
1005 **(J)** HCR *in situ* hybridization for *syt11b* in SC cross-sections of Tg(*vglut2a*:RFP; *gad1b*:GFP)
1006 zebrafish at 0, 1 and 3 wpi. Dotted lines delineate central canal edges. Arrowheads point to
1007 overlapping of *syt11b* transcripts with either *vglut2a* or *gad1b*. **(K)** Quantification of *syt11b*
1008 transcripts within *vglut2a*$^+$ and *gad1b*$^+$ neurons at 0, 1 and 3 wpi (ANOVA p-value <0.0001). *syt11b*
1009 signal outside either of these neurotransmitter populations was also quantified. SC cross sections
1010 at 450 µm rostral to the lesion were analyzed. Solid circles and polygons in the bar charts indicate
1011 individual animals and sample sizes are indicated in parentheses. Brown-Forsythe and Welch
1012 ANOVA test was performed in B, C, E, F, G, H, and I with Dunnett's T3 multiple comparisons test
1013 performed across different time points with 95% CI. Two-way ANOVA was performed in K with
1014 Tukey's multiple comparisons test with 95 % CI. * p≤0.05, ** p ≤0.01, *** p≤0.001. Scale bars, 50
1015 µm.

Figure 7

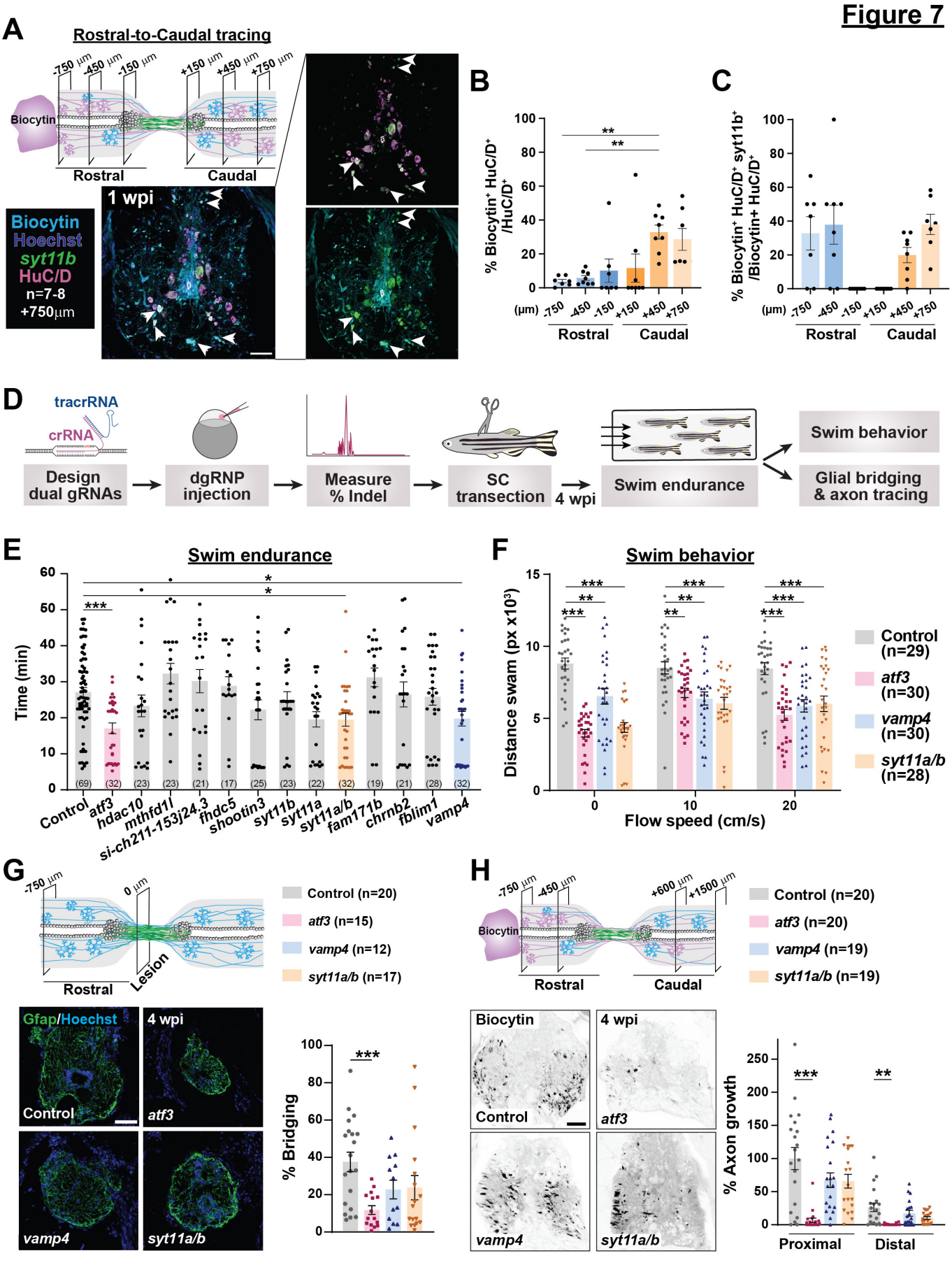
A
Rostral-to-Caudal tracing
-750 µm
-450 µm
-150 µm
+150 µm
+450 µm
+750 µm
Biocytin
Rostral
Caudal
1 wpi
Biocytin
Hoechst
syt11b
HuC/D
n=7-8
+750µm
B
% Biocytin+ HuC/D+ /HuC/D+
(µm)
Rostral
Caudal
C
% Biocytin+ HuC/D+ syt11b+ /Biocytin+ HuC/D+
D
tracrRNA
crRNA
Design dual gRNAs
dgRNP injection
Measure % Indel
SC transection
4 wpi
Swim endurance
Swim behavior
Glial bridging & axon tracing
E
Swim endurance
Time (min)
Control
atf3
hdac10
mthfd1l
si-ch211-153j24.3
fhdc5
shootin3
syt11b
syt11a
syt11a/b
fam171b
chrnb2
fblim1
vamp4
F
Swim behavior
Distance swam (px x10³)
Flow speed (cm/s)
Control (n=29)
atf3 (n=30)
vamp4 (n=30)
syt11a/b (n=28)
G
-750 µm
0 µm
Rostral
Lesion
Control (n=20)
atf3 (n=15)
vamp4 (n=12)
syt11a/b (n=17)
Gfap/Hoechst
4 wpi
Control
atf3
vamp4
syt11a/b
% Bridging
H
-750 µm
-450 µm
+600 µm
+1500 µm
Biocytin
Rostral
Caudal
Control (n=20)
atf3 (n=20)
vamp4 (n=19)
syt11a/b (n=19)
Biocytin
4 wpi
Control
atf3
vamp4
syt11a/b
% Axon growth
Proximal
Distal

1016 **Figure 7. Tracing and CRISPR/Cas9 mutagenesis of iNeuron marker genes in zebrafish. (A-**
1017 **C)** Rostral-to-caudal tracing of neurons at 1 wpi. Biocytin was applied 4 mm rostral to the lesion
1018 and co-labeled with *syt11b* HCR *in situ* hybridization and HuC/D staining. SC cross sections 750
1019 mm caudal to the lesion are shown in A. Dotted lines delineate central canal edges. The profiles
1020 of Biocytin-labeled neurons (Biocytin$^+$ HuC/D$^+$) were normalized to total neurons (HuC/D$^+$) in B.
1021 The profiles of Biocytin-labeled neurons (Biocytin$^+$ HuC/D$^+$) were normalized to total neurons
1022 (HuC/D$^+$) in B. The profiles of Biocytin-labeled iNeurons (Biocytin$^+$ HuC/D$^+$ *syt11b*$^+$) were
1023 normalized to traced neurons (Biocytin$^+$ HuC/D$^+$) in C. ANOVA p-values are 0.0029 for A and
1024 0.0011 for B. **(D)** Pipeline for CRISPR/Cas9 mutagenesis of iNeuron marker genes for
1025 regeneration assessment. CRISPR/Cas9 dual-guide ribonucleic protein duplexes targeting
1026 iNeuron genes injected into one-cell zebrafish embryos. Mutagenesis efficiency was confirmed
1027 by capillary electrophoresis and animals with >90% mutagenesis were used for SCI. Swim
1028 endurance, swim behavior and histological regeneration assays were performed at 4 wpi. **(E)**
1029 Functional recovery in CRISPR/Cas9 targeted animals 4 wpi. For each group of targeted animals,
1030 uninjected siblings were subjected to SCI and swim endurance assays (ANOVA p-value <0.0001).
1031 Dots represent individual animals. **(F)** Swim behavior assays in CRISPR/Cas9 targeted animals
1032 4 wpi (ANOVA p-value <0.0001). Swim distance was tracked under water current velocities of 0,
1033 10 and 20 cm/s. **(G)** Glial bridging in CRISPR/Cas9 targeted animals at 4 wpi. Representative
1034 immunohistochemistry shows the Gfap$^+$ bridge at the lesion site in *atf3, vamp4* and *syt11a/b*
1035 crispants relative to controls. Percent bridging represents the cross-sectional area of the glial
1036 bridge at the lesion site (0 μm) relative to the intact SC 750 μm rostral to the lesion (ANOVA p-
1037 value: 0.0049). **(H)** Anterograde axon tracing in CRISPR/Cas9 targeted animals at 4 wpi. Biocytin
1038 axon tracer was applied rostrally and analyzed at 600 μm (proximal) (ANOVA p-value <0.0001)
1039 and 1500 μm (distal) (ANOVA p-value: 0.0006) caudal to the lesion. Representative traces of
1040 biocytin are shown at the proximal level. Axon growth was first normalized to the extent of biocytin
1041 at 450 and 750 μm rostral to the lesion, and then to labeling in wild-type controls at the proximal
1042 level. Solid circles and polygons in the bar charts indicate individual animal and sample sizes are
1043 indicated in parentheses. Brown-Forsythe and Welch ANOVA test was performed in B, E and G
1044 with Dunnett's T3 multiple comparisons test performed across different time points with 95% CI.
1045 Two-way ANOVA with Dunnett's multiple comparisons test (95% CI) was performed in C. *
1046 p≤0.05, ** p ≤0.01, *** p≤0.001. Scale bars, 50 μm.